J. Fluid Mech. (1992), vol. 242, pp. 655–700
Printed in Great Britain

Direct simulation of particle dispersion in a decaying isotropic turbulence

By S. ELGHOBASHI AND G. C. TRUESDELL
Mechanical and Aerospace Engineering Department, University of California, Irvine, CA 92717, USA

(Received 26 July 1990 and in revised form 13 March 1992)

Dispersion of solid particles in decaying isotropic turbulence is studied numerically. The three-dimensional, time-dependent velocity field of a homogeneous, non-stationary turbulence was computed using the method of direct numerical simulation (DNS). A numerical grid containing 96^3 points was sufficient to resolve the turbulent motion at the Kolmogorov lengthscale for a range of microscale Reynolds numbers starting from $R_\lambda = 25$ and decaying to $R_\lambda = 16$. The dispersion characteristics of three different solid particles (corn, copper and glass) injected in the flow, were obtained by integrating the complete equation of particle motion along the instantaneous trajectories of 22^3 particles for each particle type, and then performing ensemble averaging. The three different particles are those used by Snyder & Lumley (1971), referred to throughout the paper as SL, in their pioneering wind-tunnel experiment. Good agreement was achieved between our DNS results and the measured time development of the mean-square displacement of the particles.

The simulation results also include the time development of the mean-square relative velocity of the particles, the Lagrangian velocity autocorrelation and the turbulent diffusivity of the particles and fluid points. The Lagrangian velocity frequency spectra of the particles and their surrounding fluid, as well as the time development of all the forces acting on one particle are also presented. In order to distinguish between the effects of inertia and gravity on the dispersion statistics we compare the results of simulations made with and without the buoyancy force included in the particle motion equation. A summary of the significant results is provided in §7 of the paper.

The main objective of the paper is to enhance the understanding of the physics of particle dispersion in a simple turbulent flow by examining the simulation results described above and answering the questions of how and why the dispersion statistics of a solid particle differ from those of its corresponding fluid point and surrounding fluid and what influences inertia and gravity have on these statistics.

1. Introduction

Since the pioneering experiment of Snyder & Lumley (1971; hereinafter referred to as SL), many attempts by various researchers have been made to predict numerically the particle dispersion statistics observed in the experiment. A drawback common to most of these attempts was that the instantaneous velocity of the fluid surrounding the particle was determined from the time-averaged Navier–Stokes equations together with a turbulence closure model, and an assumed shape of the p.d.f. of the velocity. Furthermore, major simplifying assumptions were needed to prescribe the residence time of the particle in a large-scale turbulence eddy. In fact some analytical

studies assumed that the particle resides permanently in an eddy during its lifetime. The method of direct numerical simulations (DNS), on the other hand, provides a modelling-free, three-dimensional, instantaneous velocity field for the fluid in simple turbulent flows. This velocity field can be used to calculate the three-dimensional trajectory of a particle from which the dispersion statistics can be obtained. This is the approach we adopted in the work to be presented here.

Although DNS has been used in the past to compute particle dispersion in turbulent flows (Riley & Patterson 1974; Squires & Eaton 1991), none of the published studies simulated the SL experiment. Thus, one of the aims of the present paper is to illustrate in some detail how DNS can be used to simulate a 'real' laboratory experiment of particle dispersion in a simple turbulent flow. Because of the lower Reynolds number in DNS, certain scaling of the relevant timescales is necessary. Another aim is to provide detailed physical information that can be obtained only from DNS, about the flow and particle statistics for the SL experiment. For example, the time development of the mean square relative velocity and all the forces acting on the particle and dispersion statistics of fluid point and surrounding fluid were not and could not have been provided by SL. In addition, dispersion in zero gravity environment of the same particles that were used in the experiment of SL is examined to distinguish between the effects of inertia and crossing trajectories. Therefore the results presented in this paper complement those of SL and provide a rather complete set of data for validating analytical and simpler numerical models of turbulent dispersion of solid particles.

The work to be described here is part of a study of particle dispersion and turbulence modulation in unsheared and sheared turbulence. Preliminary results of this work have been presented in Elghobashi & Truesdell (1989*a*, *b*, 1991). The present paper considers only the one-way coupling case, i.e. particle dispersion without turbulence modulation. The study of two-way coupling is presented elsewhere (Elghobashi & Truesdell 1991). The following summarizes other published DNS studies of particle dispersion.

Riley & Patterson (1974) were the first to present a computer simulation of 'small' particle autocorrelation and mean-square displacement in a numerically integrated, decaying isotropic flow field. A 'small' particle was defined as that whose diameter and response time are less than the Kolmogorov lengthscales and timescales. The fluid Eulerian velocity field was obtained by direct numerical simulation of turbulence in a cubical volume (32^3 grid points), with an initial microscale Reynolds number $R_\lambda = 23$. The trajectories of 432 particles were obtained from the numerical solution of the equation of particle motion including only the Stokes drag. As expected, their simulation showed that in the absence of gravity, increasing the response time of the particle increased its velocity autocorrelation coefficient. The absence of the gravity term from the particle motion equation eliminates the effects of crossing trajectories (Yudine 1959), and thus increases the velocity autocorrelation coefficient as shown by Reeks (1977) and Wells & Stock (1983).

Squires & Eaton (1991) studied particle dispersion in stationary (forced) and decaying isotropic turbulence using DNS. The simulation of decaying turbulence used 128^3 grid points, and R_λ decayed from 43.2 to 17.5. They studied the dispersion statistics of six different (response time) particles, with each simulation tracking the trajectories of 4096 particles.

McLaughlin (1989) computed particle trajectories in a numerically simulated vertical channel flow, with $16 \times 64 \times 65$ grid points, to study particle deposition on the wall. The equation of motion of the particle included the Stokes drag and

Saffman lift force, but not the gravity, virtual mass, and Basset history terms. It was found that although the magnitude of Saffman lift force was less than that of the component of Stokes drag normal to the wall, the impulse provided by the lift force had a significant effect on particle deposition within the viscous sublayer. The reason is that in this region the normal component of fluid velocity is relatively small. The Saffman lift force tends to trap the particles within the viscous sublayer.

The above review shows that in previous DNS studies of particle dispersion, comparison between DNS results and the experimental measurements of SL was not made. In addition, the dispersion statistics in our simulation are obtained from a larger number of realizations, 10648 ($= 22^3$) particles, than in previous studies.

It was planned at the beginning of this study to simulate the experiment of Wells & Stock (1983) in addition to that of SL. However, in the former, the particles were introduced into the wind tunnel upstream of the turbulence-generating grid, without providing information on the relative velocity of the particles downstream of the grid. This information is needed to start the computation of the particle trajectory in our simulation. SL, on the other hand, provided such information by stating that 'the particles were ejected at the wind tunnel centreline 20 mesh lengths from the grid with a mean velocity the same as the tunnel speed'. Of course, in DNS, the instantaneous, not the mean, values are needed for prescribing the initial conditions. Therefore the assumption of equal instantaneous velocity of particle and fluid at the particle injection position is adopted here.

Sections 2, 3 and 4 describe the governing equations and the numerical method. Section 5 discusses the necessary scaling of timescales in our simulation in order to mimic the experimental conditions for particle dispersion and presents the properties of the solid particles. Section 6 discusses the results. The conclusions are presented in §7.

2. Equation of particle motion

The instantaneous velocity, v_i, in the x_i-direction (figure 1), of each particle is obtained by time integration of the following Lagrangian equation of particle motion:

$$\begin{aligned} m_p(\mathrm{d}v_i/\mathrm{d}t_p) = {} & m_p F(u_i - v_i) && \text{viscous and pressure drag force} \\ & + m_f(\mathrm{D}u_i/\mathrm{D}t) && \text{force due to fluid pressure gradient and viscous stresses} \\ & + \tfrac{1}{2}m_f(\mathrm{D}u_i/\mathrm{D}t - \mathrm{d}v_i/\mathrm{d}t_p) && \text{inertia force of added mass} \\ & + 6a^2(\pi\rho\mu)^{\frac{1}{2}} \int_{t_{p_0}}^{t_p} \frac{\mathrm{d}/\mathrm{d}\tau(u_i - v_i)}{(t_p - \tau)^{\frac{1}{2}}}\,\mathrm{d}\tau && \text{viscous force due to unsteady relative acceleration (Basset)} \\ & + (m_p - m_f)g_i && \text{buoyancy (or gravity) force.} \end{aligned} \tag{1}$$

Equation (1) describes the balance of forces acting on the particle as it moves along its trajectory. The term on the left-hand side is the inertia force acting on the particle due to its acceleration. F is the inverse response time of the particle. The response time is the time for momentum transfer due to drag. F is calculated from:

$$F = 1/\tau_p = \left(\frac{3}{8a}\right) C_D \left(\frac{\rho}{\rho_p}\right) |u_i - v_i|, \tag{2}$$

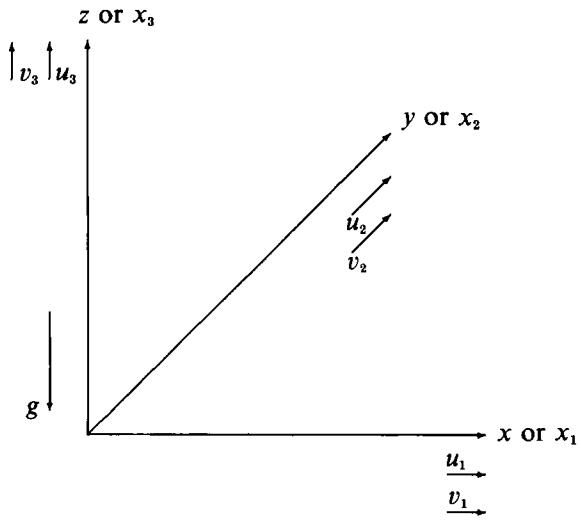

FIGURE 1. Coordinates x_i, fluid velocity components u_i and particle velocity components v_i.

and:

a particle radius,

C_D drag coefficient, function of R_p,

$\frac{d}{dt_p}$ derivative with respect to time following the moving particle,

$\frac{Du_i}{Dt}$ total acceleration of the fluid as seen by the particle,

$$\frac{Du_i}{Dt} = \left[\frac{\partial u_i}{\partial t} + u_j \frac{\partial u_i}{\partial x_j}\right] \text{ evaluated at the particle position } \boldsymbol{x}_p,$$

g_i gravitational acceleration in x_i-direction,

m_f mass of the fluid displaced by the particle, $= m_p(\rho/\rho_p)$,

m_p mass of the particle,

R_p Reynolds number of particle, $= 2a\rho|u_i - v_i|/\mu$,

u_i instantaneous velocity of the fluid at the particle location,

v_i instantaneous velocity of the particle in the x_i-direction,

μ dynamic viscosity of fluid,

ρ fluid density,

ρ_p particle density,

τ_p particle response time.

Both u_i and v_i are measured with respect to a coordinate system that is moving with a constant mean stream velocity in the vertical (x_3)-direction, i.e. opposite to that of the gravitational acceleration. This simple transformation removes the effects of mean advection and allows us to examine the influence of turbulent fluctuations on solid and fluid particle dispersion which is of main interest here.

Equation (1) has a long history dating back to Stokes (1851), followed by Basset (1888), Boussinesq (1903) and Oseen (1927). It has undergone extensive modifications starting with Tchen (1947), followed by Corrsin & Lumley (1956), Lumley (1957), Maxey & Riley (1983) and Auton (1983) among others. It is well known that (1) has

no exact solution, except for a trivial case, even in its simplest form in which all but the first term on the right-hand side vanishes. This is due to the nonlinearity originating from the need to evaluate the fluid velocity, u_i, at the yet unknown particle position. The trivial case that has an exact solution is that of an invariant and uniform fluid velocity, i.e. the flow cannot be turbulent.

It should be noted that if the particle Reynolds number R_p is not small, permitting a Stokes approximation, no exact explicit equation of motion is known (Lumley 1978). Of course the flow around the particle is determined by the Navier–Stokes equations, but the resulting drag is not a simple function of the relative velocity.

Lumley (1978) examined the validity of the particle equation and showed that there are three requirements for it to be used in a turbulent flow:

(i) R_p based on the fluctuating relative velocity should be less than 0.5.

(ii) The flow in the vicinity of the particle should be at most homogeneous shear, which approximately means that $d/\eta < \frac{1}{6}$, where d is the particle diameter and η is the Kolmogorov lengthscale, $\eta = (\nu^3/\epsilon)^{\frac{1}{4}}$, where ϵ is the dissipation rate of turbulence energy.

(iii) For $R_p \leqslant 10$, the wake can be considered stable; the flow around the particle can be assumed quasisteady, and the drag will be aligned with the relative velocity vector. It can be shown that these conditions approximately mean that $d/\eta < 4$ or $(d/\eta)^2 \ll 4R_p$.

Of the above three requirements, (i) is the most restrictive. We have monitored the values of R_p of all the particles during the simulation. The R_p values for the heaviest particle (solid glass with 87 μm diameter used by Snyder & Lumley (1971)) remained always below 1.46, and for the lighter particles (corn with 87 μm diameter) remained always below 0.74. It should be mentioned that during the simulations the ratio d/η remained < 0.12, and $0.33 \leqslant \tau_p/\tau_K \leqslant 1.98$ for all the particles used, where τ_K is the Kolmogorov timescale, defined as $\tau_K = (\nu/\epsilon)^{\frac{1}{2}}$.

Although the magnitude of some of the forces on the right-hand side of (1) may be negligible compared to the drag and gravity forces in the flow considered, we decided to retain all the forces in the equation to examine their transient behaviour along the particle trajectory, as will be discussed later in §6.7.

3. Computation of particle trajectories

The integration of (1), via a second-order Adams–Bashforth scheme provides the new velocity, $v_i(t)$, in the x_i-direction for each particle as a function of time. The new position, $x_{p,i}(t_n)$ is calculated from:

$$x_{p,i}(t_n) = x_{p,i}(t_{n-1}) + \tfrac{1}{2}\Delta t[v_i(t_n) + v_i(t_{n-1})], \tag{3}$$

where t_{n-1} is the time at the previous timestep, and $\Delta t = t_n - t_{n-1}$.

The fluid velocity $u_i[x_{p,i}(t)]$ at the particle location (initially, the velocities of the coincident fluid and particle are assumed equal), which is needed to integrate (1) is obtained by a fourth-order accurate, two-dimensional, four-point Hermitian cubic polynomial interpolation scheme between the adjacent Eulerian fluid velocity values. This scheme is applied in the three coordinate directions at the particle location.

We have compared the accuracy of this scheme with twelve others (Truesdell 1989) including linear interpolation, Lagrange with 36 points, midpoint with 21 points, midplane with 24 points and third-order Taylor-series with 13 points of Yeung & Pope (1988). It was concluded that the fourth-order accurate Hermitian scheme is

superior to the other schemes regarding the combination of accuracy and computational economy. Balachandar & Maxey (1989) used a fourth-order Hermitian scheme in two directions followed by a Fourier interpolation in the third direction. The accuracy of our scheme compares well with theirs.

A number of solid particles is selected to compute the particle dispersion statistics. The number of particles should be large enough to obtain an ensemble average of the independent realizations of the random dispersion process. It can be shown from the central limit theorem that the relative error in performing the ensemble averaging varies as $(M)^{-\frac{1}{2}}$, where M is the number of independent realizations. For $M = 2000$ the error is about 3%, and for $M = 14000$ the error is about 1%, i.e. the gain in accuracy diminishes as we increase the number of particles. In §§6.2 and 6.3 we compare the simulation results of 8^3, 16^3, 22^3 and 32^3 particles and show that the results of 22^3 (= 10648) and 32^3 (= 32768) particles are virtually indistinguishable within the plotting accuracy. Thus for the results presented here we used 22^3 particles without much loss of accuracy.

We start the computation of particle trajectories by uniformly distributing a number of particles, e.g. 22^3, within the computational box where there are, for example, 884736 possible locations in the 96^3 grid. The initial velocity of each particle is assumed equal to the fluid velocity at the same location. We then integrate (1) in the three coordinate directions to obtain the subsequent particle velocity, and calculate the new position from (3). The magnitude of the timestep Δt is bounded on one hand by the available computer disk space and on the other by the resolution needed to compute accurate trajectories. This accuracy requires Δt to be much smaller than τ_p, and consequently the three-dimensional velocity field of the fluid needs to be stored at intervals equal to Δt, which is larger than the timestep used in integrating the Navier–Stokes equations for the fluid. The smaller Δt, the higher is the storage frequency and the larger is the disk space required. The results presented in this paper were obtained with Δt ranging between a third and a half τ_p. The disk space required to store the three velocity components of the fluid at the 96^3 grid points was 10 megabytes per timestep, and a complete particle trajectory required one gegabyte of disk space.

Tests were made by reducing Δt to a quarter of the value used here, and the resulting difference in the dispersion statistics was less than 1%.

4. Numerical simulation of grid-generated turbulence

We solve the exact time-dependent, three-dimensional continuity and Navier–Stokes equations under periodic boundary conditions in a cubical domain with side length L; $L = 1$. The domain moves with the constant mean stream velocity in the vertical positive x_3-direction, thus the dependent variables of the four governing equations are the instantaneous fluctuations of the three velocity components, u_i, and the pressure. The fluid is incompressible and has a constant kinematic viscosity, ν.

The equations are discretized in an Eulerian framework using a second-order finite-difference technique on a staggered grid containing N^3 points. N is an even number of points which are equispaced within the length L in each of three coordinate directions. The Adams–Bashforth scheme is used to integrate the equations in time. Pressure is treated implicitly, and is obtained by solving the Poisson equation in finite-difference form using a fast Poisson solver. More details about the numerical method are discussed by Gerz, Schumann & Elghobashi (1989).

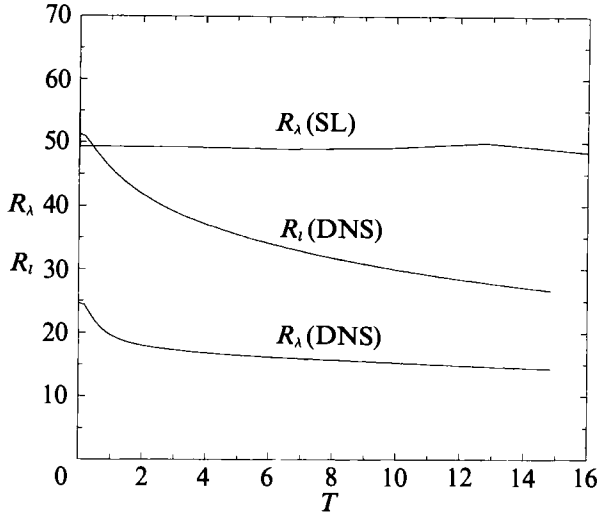

FIGURE 2. Time development of microscale Reynolds numbers R_λ for the simulation (DNS) and Snyder & Lumley's experiment (SL), and integral scale Reynolds number R_l.

The initialization algorithm ensures, for a prescribed energy spectrum, that the initial random velocity field is isotropic, periodic in the three spatial directions, and divergence-free with respect to the discretized form of the continuity equation. It also ensures that the cross-correlation spectra, $R_{ij}(k)$, satisfy the realizability constraints (Schumann 1977).

The energy spectrum $E(k,0)$ at dimensionless time $T = 0$ is prescribed by:

$$E(k,0) = (3u_0^{*2})(1/2\pi)(k/k_p^2)\exp[-k/k_p], \tag{4}$$

where u_0^* is the dimensionless r.m.s. velocity (see table 1 for reference quantities), k is the wavenumber, and k_p is the wavenumber of peak energy. All the wavenumbers appearing in (4) are normalized by the lowest non-zero wavenumber, k_{min}, which equals 2π since the size of the computational domain $L = 1$, as mentioned above. The two inputs u_0^* and k_p are sufficient to specify $E(k,0)$. The dimensionless kinematic viscosity ν is calculated for a prescribed initial microscale Reynolds number, $R_{\lambda_0} = \lambda_0 u_0^*/\nu$, by solving the two equations defining λ_0 and the energy dissipation rate ϵ_0:

$$\lambda_0 = [15u_0^{*2}\nu/\epsilon_0]^{\frac{1}{2}}, \tag{5}$$

$$\epsilon_0 = 2\nu\int k^2 E(k,0)\,\mathrm{d}k. \tag{6}$$

The values of the dimensionless parameters at ($T = 0$) used in the present simulation are: $R_{\lambda_0} = 25$ (figure 2), $(k_p/k_{min}) = 6$, $u_0^* = 0.0504$ (figure 5), $\lambda_0 = 0.0238$ (figure 7), $\nu = 4.88 \times 10^{-5}$. The values of the reference length and timescales used in normalizing these quantities are listed at the end of table 1. The number of grid points is 96^3.

It should be emphasized that the spectrum (4) is appropriate for the initial period of decay (Schumann & Patterson 1978) during which R_λ remains nearly constant (Batchelor 1953) and the time exponent of energy decay is approximately equal to -1.

The spectrum introduced by Kraichnan (1970)

$$E(k) = 16(2/\pi)^{\frac{1}{2}}u_0^{*2}(k^4/k_p^5)\exp[-2(k/k_p)^2], \tag{7}$$

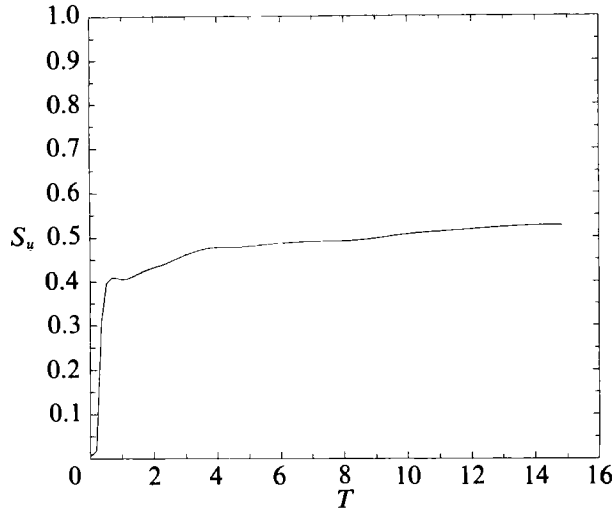

FIGURE 3. Time development of the skewness of the fluid velocity derivatives.

and used by Riley & Patterson (1974) and Balachandar & Maxey (1989) results in a much faster decay of R_λ with time than in the experiment (Schumann & Patterson 1978). The spectrum developed by Pao (1965) and used by Yeung & Pope (1988) namely

$$E(k) = k^{-\frac{5}{3}} \exp[-1.5\alpha(k\eta)^{\frac{4}{3}}], \tag{8}$$

where α is a constant, mimics the inertial subrange for $k \ll (1/\eta)$ and the universal range for $k \gg (1/\eta)$. Of course, the true inertial subrange behaviour, with significant separation between the dissipative and energy-containing wavenumbers, can only be possible at much higher values of R_λ than those achieved in direct numerical simulations at present, and thus the spectrum (8) is not suitable for our flow.

The spectrum used in our simulation, equation (4), results in an energy decay rate proportional to t^{-1} which is expected for the initial period of decay. Since solid particle dispersion depends on the decay rate of turbulent kinetic energy, it was necessary to simulate SL's rate of energy decay. The virtual origins they used to obtain a decay rate proportional to $(x/M)^{-1}$ were 16.0 and 12.0 for the vertical and lateral velocity components respectively. In our simulation, a virtual origin of a dimensionless time $T = 0.36$ was necessary to achieve a decay rate proportional to t^{-1}. With a virtual origin of $T = 0$, the decay exponent equals -1.07. Figure 2 shows the time development of R_λ in which $18 \geqslant R_\lambda \geqslant 15.9$ for the interval $2.0 \leqslant T \leqslant 7.2$ whereas R_λ in the experiment of SL remains nearly constant at an average value of 48.5 within the test section. The significance of this time interval will become clear below.

It should be emphasized that the dimensionless time T is measured from the start of the simulation of fluid turbulence.

Figure 3 displays the temporal variation of the skewness of the velocity derivative, defined as

$$S_u = \left[-\frac{1}{3}\sum_{i=1}^{3} \langle(\partial u_i/\partial x_i)^3\rangle\right] \Big/ \left[\frac{1}{3}\sum_{i=1}^{3} \langle(\partial u_i/\partial x_i)^2\rangle\right]^{\frac{3}{2}}, \tag{9}$$

and is a measure of the average rate of production of enstrophy by vortex stretching or the rate of nonlinear energy transfer from the low to high wavenumbers. Earlier measurements by Batchelor & Townsend (Batchelor 1953) show that S_u varies

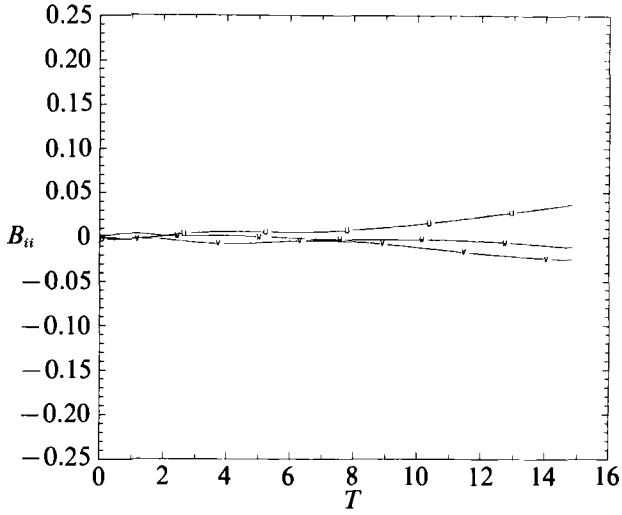

FIGURE 4. Time development of the components of the anisotropy tensor, $B_{11}(-u-)$, $B_{22}(-v-)$, $B_{33}(-w-)$.

between 0.48 and 0.33 for R_λ values between 20 and 60 respectively. Recent measurements by Mohamed & LaRue (1990) indicate the same dependence of S_u on R_λ. Figure 3 shows that S_u reaches a value of 0.4 at $T = 1.0$, indicating that fully developed turbulence was established at that time and then remains nearly constant. An additional criterion was used to determine the time at which the turbulent field was fully developed. It requires that the decay exponent, n, and the virtual origin, x_0, used in the power-law expression $\langle u^2\rangle/U^2 = A(x/M - x_0/M)^n$, should not depend on the starting position (or time) of the decay data (Mohamed & LaRue 1990). Using this criterion, it was determined that the turbulence was fully developed for $T \geqslant 2.0$, and thus the solid particles are injected at $T = 2$. The time development of S_u in isotropic turbulence computed by the spectral method of Orszag & Patterson (1972) and Schumann & Patterson (1978) is very similar to that in figure 3.

The portion of the simulation that was used for comparing the dispersion statistics from DNS with those from SL's experiment was $2.67 \leqslant T \leqslant 7.2$. The interval $2.67 \leqslant T \leqslant 15.0$ was used for the zero-gravity simulations of particle dispersion.

The anisotropy tensor of the large-scale motion is defined as:

$$B_{ij} = \frac{\langle u_i u_j\rangle}{q^2} - \tfrac{1}{3}\delta_{ij}, \tag{10}$$

where $q^2 = \langle u_i u_i\rangle$ is twice the kinetic energy of turbulence. Figure 4 shows the time development of B_{ii}. For the interval $2.67 \leqslant T \leqslant 7.2$, the maximum value of B_{ii} is less than 1% in any coordinate direction. This is lower than the value, 7.4%, observed in SL.

We also examined the temporal variation of D_{ii} which indicates the amount of anisotropy present in the small-scale turbulence, and is defined as:

$$D_{ij} = \frac{2\nu\langle u_{i,j}\, u_{j,i}\rangle}{\epsilon} - \tfrac{1}{3}\delta_{ij}, \tag{11}$$

where $\epsilon = 2\nu\langle u_{i,k}\, u_{i,k}\rangle$ is the dissipation rate of turbulence kinetic energy. For the interval $2.67 \leqslant T \leqslant 7.2$ the maximum value of D_{ii} is less than 1% in any coordinate direction and over the total simulation it is less than 2%.

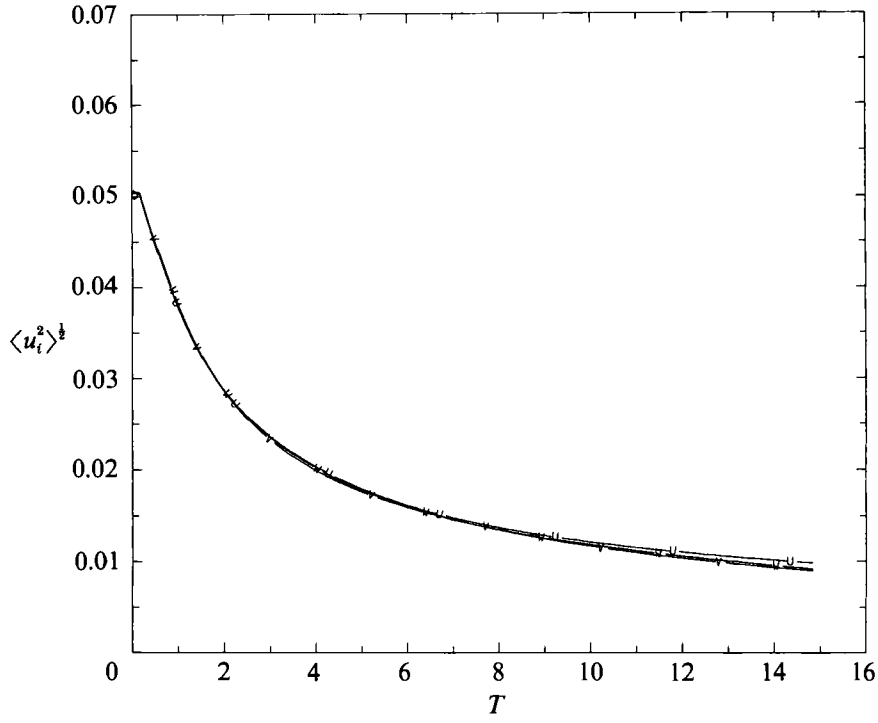

FIGURE 5. Time development of the root-mean-square fluid velocity. $(\langle u_1^2 \rangle)^{\frac{1}{2}}$ $(\langle u_2^2 \rangle)^{\frac{1}{2}}$, $(\langle u_3^2 \rangle)^{\frac{1}{2}}$ or $(-u-)$, $(-v-)$, $(-w-)$.

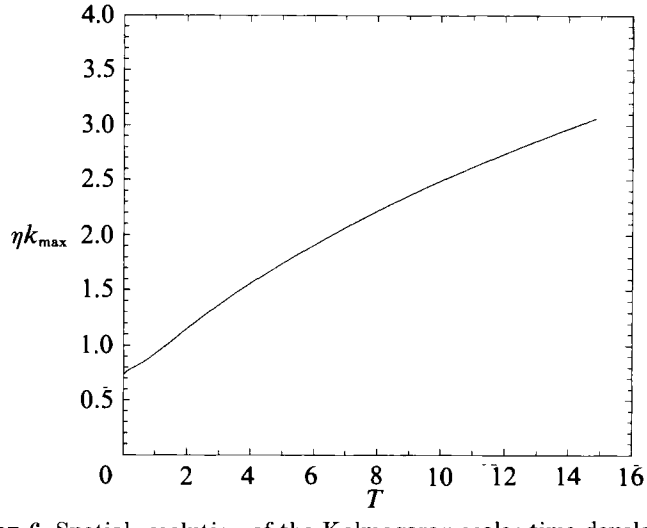

FIGURE 6. Spatial resolution of the Kolmogorov scale: time development of $\eta k_{\max}$.

The behaviour of B_{ii} described above can be seen also in figure 5 which shows the temporal variation of the three components of the r.m.s. velocity. For the interval $2.67 \leqslant T \leqslant 7.2$ the flow is highly isotropic. At the end of the simulation the $u_{1,\mathrm{rms}}$ is slightly greater than the $u_{2,\mathrm{rms}}$ or $u_{3,\mathrm{rms}}$.

The ability of the simulation to resolve the motion at the smallest turbulence scales is measured by the dimensionless quantity $\eta k_{\max}$, where $k_{\max}$ is the highest

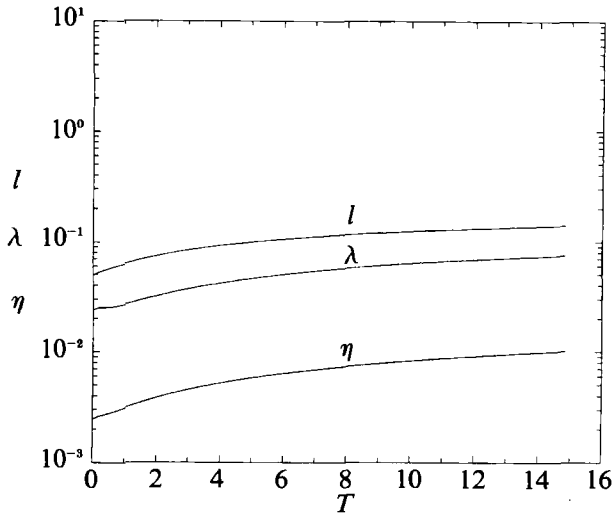

FIGURE 7. Time development of non-dimensional lengthscales: l, integral lengthscale; λ, Taylor microscale; η, Kolmogorov lengthscale.

resolved wavenumber ($= 2\pi(\frac{1}{2}N)$). The numerical simulations of Yeung & Pope (1988) indicate that the smallest scales are captured if $\eta k_{\max} \geqslant 1$. In our simulations $1.15 \leqslant \eta k_{\max} \leqslant 2.1$ for $2.0 \leqslant T \leqslant 7.2$ and increases to 3.08 at $T = 15.0$ as displayed in figure 6.

The time development of the non-dimensional integral-, Taylor-, and Kolmogorov-lengthscales is shown in figure 7. These scales are calculated directly from the three-dimensional spectra of the energy $E(k, t)$ and dissipation $\epsilon(k, t)$. The figure shows that the ratio (l/η) of the largest to smallest lengthscales is in the range $20 \geqslant l/\eta \geqslant 17.4$ for $2.0 \leqslant T \leqslant 7.2$. During this period R_l decays from 44 to 33 (figure 2), resulting in $(l/\eta) \approx 1.2R_l^{\frac{3}{4}}$ as expected.

5. Particle properties and scaling

The particles selected for the present study are three (corn pollen, solid glass and copper) of the four used by Snyder & Lumley (1971) since one of our objectives was to reproduce numerically the dispersion statistics measured by SL. The hollow glass particle was not included in our study because of a reported considerable error in its experimental data. SL stated that 'as much as 40% of the energy of the hollow glass beads could have been lost due to the low sampling rate'.

Now, the Reynolds number, R_λ, in our simulation is lower than in the experiment of SL as shown in figure 2. The figure shows that $R_\lambda = 18$ at the dimensionless time $T = 2$ when the skewness of the velocity derivative reaches 0.43. In the experiment of SL, R_λ remains at a value of about 48.5 throughout the test section, where ours decays to 15.9. In the experiment, the r.m.s. velocity decay rate nearly equals the growth rate of the Taylor microscale, λ, whereas in our simulation, because of the lower R_λ, the Taylor microscale grows at a slower rate than that of the r.m.s. velocity decay. Thus the effect of the local fluid acceleration on a particle in the simulation will be different from that on an identical particle in the experiment. Therefore it is necessary to ensure that the ratio $(\tau_{p,0}/\tau_{f,0})$ has the same value in the simulation and experiment, where $\tau_{f,0}$ is the turbulence timescale or eddy turnover time $\tau_{f,0} = l_0/u_0$ at the time of starting the dispersion statistics. And since gravity provides the only

external force in (1), i.e. it is independent of the turbulence properties, we must scale the gravitational acceleration in the simulation so that its effect relative to that of fluid acceleration be the same as in the experiment.

Accordingly, it is necessary to satisfy for each of the three particles studied in our simulation, the following two scaling conditions at the location (or time) of the first experimental station $x/M = 68.4$:

$$[\tau_{p,0}/\tau_{f,0}]_{DNS} = [\tau_p/\tau_{f,0}]_{EXPT}, \tag{12}$$

$$[\tau_{g,0}/\tau_{f,0}]_{DNS} = [\tau_g/\tau_{f,0}]_{EXPT}, \tag{13}$$

where $\tau_{g,0} = d/v_{t,0}$ is the 'drift timescale' and $v_{t,0} = g^*\tau_{p,0}$ is the initial drift velocity. The gravitational acceleration in the simulation, g^*, is calculated from (13). The subscript 0 denotes the dimensionless time $T = 2.67$ at which we start calculating the dispersion statistics as will be discussed in detail in §6.1. The drift timescale τ_g is the time spent by the particle to drift, due to gravity, a distance equal to its diameter. The ratio between τ_g and the eddy turnover time τ_f signifies the effect of crossing trajectories as will be discussed later in §6.2. Two particles with different drift timescales, τ_{g1} and τ_{g2}, existing initially at the same point in a turbulent eddy will cross the boundary of that eddy to another, under gravity effect, at different times. The value of g^* obtained from (13) is nearly the same for the three particles studied (the maximum difference is about 5%), and thus the average of the three values was used in all simulations.

It is important here to discuss why scaling of the drift timescale should be made with respect to the eddy turnover time, i.e. the timescale of the large-scale motion and not that of the Kolmogorov scale. Of course, the fact that the particle diameter is smaller than η may intuitively suggest that scaling should be with respect to the latter. However, τ_p is of the same order of τ_K, and the ratio τ_p/τ_K exceeds 1 in the experiment and our simulation (table 1), especially during the important initial period of dispersion. On the other hand, the ratio τ_p/τ_f is always less than 1 throughout the simulation and in the experiment. In other words, deformation of large eddies (e.g. stretching and bending) occurs at frequencies small enough for the particles to respond to, and displace with, much more readily than they do with the higher frequencies of the small-scale motion. This behaviour is evident in figure 13 showing the Lagrangian velocity frequency spectra of the particles and surrounding fluid, as will be discussed in §6.6. Thus, a large eddy 'carries' the small particles along, unless their τ_p is large enough that gravity pulls them out of that eddy to 'cross' into a neighbouring eddy. The strong dependence of particle dispersion on the large-scale motion is also confirmed by the studies of Reeks (1977), Lumley (1978), Crowe, Chung & Trout (1988) and Squires & Eaton (1991). Thus, fluid motion at the Kolmogorov scale has negligible effect on particle displacement, and should not be used for scaling the acceleration.

The lengthscale, l_0, used in calculating $\tau_{f,0}$ is obtained from the three-dimensional energy spectrum according to:

$$l(t) = \frac{1}{2u_{rms}^2(t)} \int \frac{E(k,t)}{k} \mathrm{d}k. \tag{14}$$

The three-dimensional energy spectrum $E(k,t)$ is calculated at any time t by the integration of the Fourier transform of the trace of the velocity correlation tensor over a spherical shell of radius k which is the magnitude of the wavenumber vector $\boldsymbol{k}$.

		Corn pollen	Solid glass	Copper
Diameter (μm)	(d)	87	87	46.5
Density ratio	(ρ_p/ρ_f)	1000	2500	8900
Initial τ_p (s) (SL)	(τ_p)	0.020	0.045	0.049
Initial τ_p (s) (DNS)	($\tau_{p,0}$)[a]	0.027	0.061	0.067
Ratio of initial timescales				
(DNS) and (SL, $x/M = 68.4$)	($\tau_p/\tau_{f,0}$)	0.090	0.203	0.221
(DNS) and (SL, $x/M = 68.4$)	($\tau_g/\tau_{f,0}$)[b]	2.0×10^{-3}	8.9×10^{-4}	4.4×10^{-4}
Ratio of initial velocities				
(DNS)	($v_{t,0}/u_0$)	3.16	6.69	7.57
Ratio (τ_p/τ_K) (min, max)				
(DNS)	(τ_p/τ_K)	0.33, 0.81	0.74, 1.82	0.81, 1.98
(SL)	(τ_p/τ_K)	0.66, 1.88	1.49, 4.23	1.63, 4.62
Lengthscale ratio (min, max)				
(DNS)	(d/η)	0.077, 0.121	0.073, 0.115	0.040, 0.063
(SL)	(d/η)	0.126, 0.212	0.126, 0.212	0.067, 0.113
Maximum Reynolds number	(R_p)[c]	0.735	1.46	0.936

[a] 'Initial' or subscript '0' denotes time at $T = 2.67$, where T is non-dimensional time: T = real time/reference time, where: Reference length = 0.1859 m, Reference velocity = 1.741 m/s, resulting in Reference time = 0.106 78 s, and Reference kinematic viscosity = 0.323 65 m²/s.

[b] $\tau_{g,0} = d/v_{t,0}$, $\tau_{f,0} = l_0/u_0 = 2.825$ (or 0.302 s), $l_0 = 0.0755$ and $u_0 = 0.0267$.

[c] $R_p = d|u_f - v_f|/\nu$ observed for all particle trajectories.

TABLE 1. Particle properties and flow parameters

Table 1 lists the values of the significant particle and fluid properties in both the simulation and experiment at $T = 2.67$. It should be noted that in DNS, the instantaneous value of τ_p is not a constant, instead it is calculated from (2) throughout the simulation.

6. Results

In this section we present the results of the numerical simulations and, whenever possible, compare them with the experimental data of SL. The dispersion statistics are presented for the solid particles, their surrounding fluid and their corresponding fluid points.

A *fluid point* is defined as the fluid particle that coincides with the centre of the solid particle at the injection time, t_{inj}. Therefore a fluid point is uniquely defined by the initial position of the corresponding solid particle, and its identity is preserved throughout its unsteady motion.

The *surrounding fluid*, on the other hand, is the local 'host' fluid that exists around the solid particle at each position along its trajectory, and thus the identity of the surrounding fluid varies as many times as the number of spatial positions visited by the solid particle.

We discuss in the following subsections how and why the dispersion statistics of a solid particle differ from those of its corresponding fluid point and surrounding fluid. The statistics include the mean-square relative velocity, velocity autocorrelations, mean-square displacement, turbulent diffusivity and Lagrangian velocity frequency spectrum. Comparison is also made between the developments of these statistics in gravity and zero-gravity environment. We also present the time development of all the instantaneous forces acting on one solid particle as it moves along its trajectory.

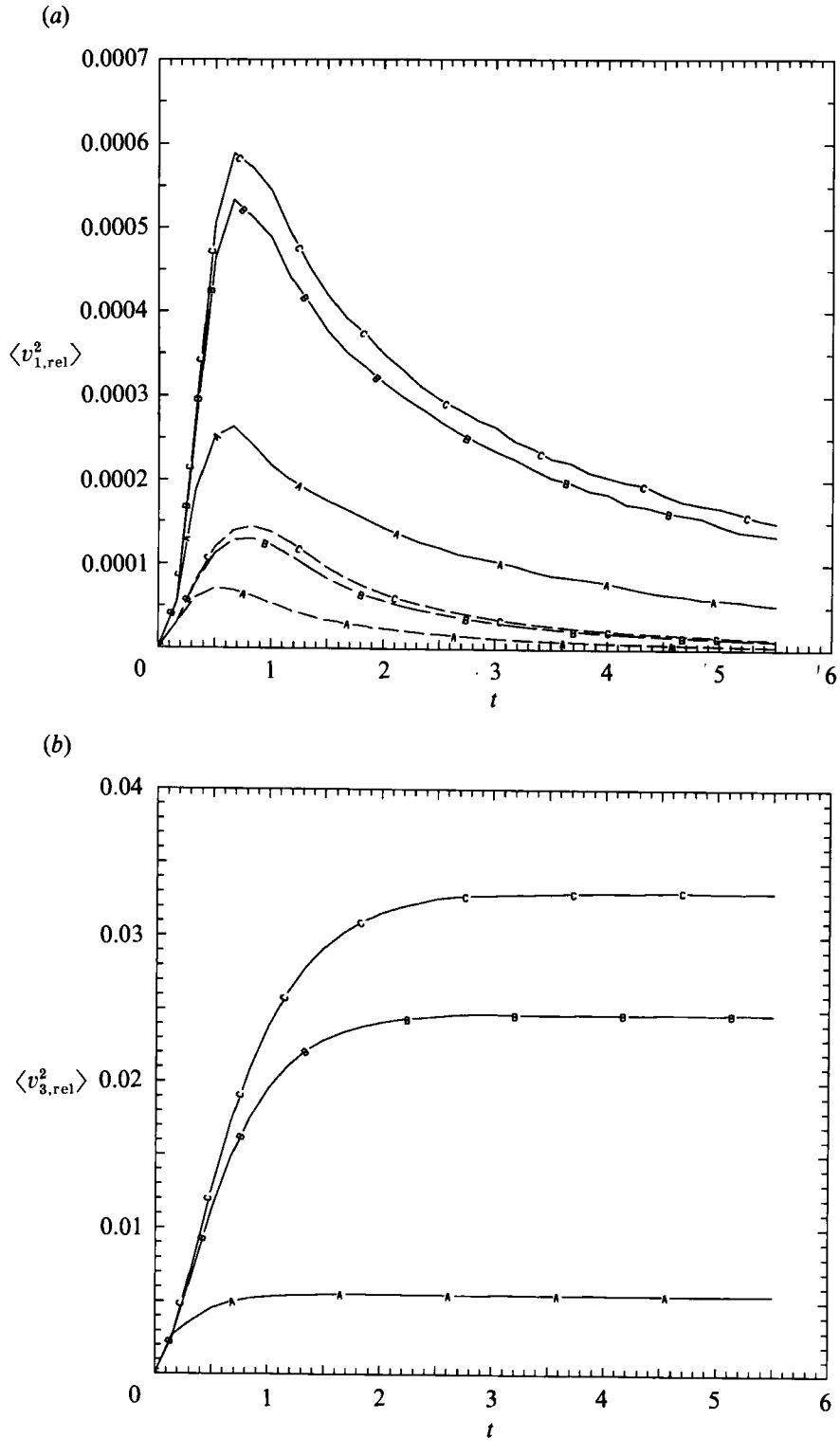

FIGURE 8(a, b). For caption see facing page.

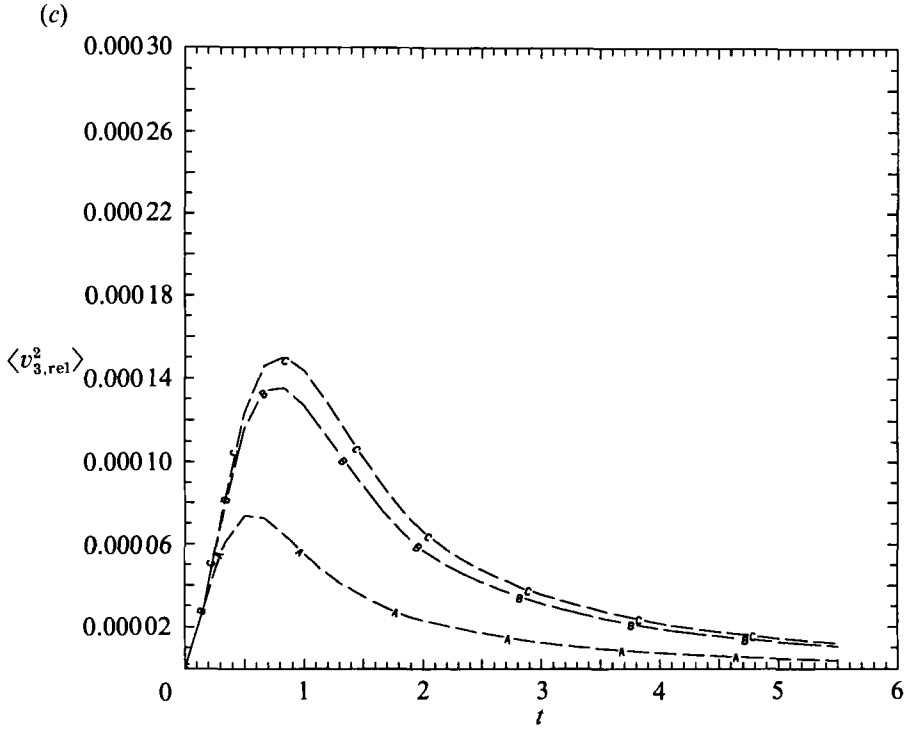

FIGURE 8. (*a*) Mean-square relative velocity of the particles in the lateral direction (x). A, corn; B, solid glass; C, copper; ——, in gravity; — —, zero gravity. (*b*) Mean-square relative velocity of the particles in gravity, in the gravity direction (z). A, corn; B, solid glass; C, copper. (*c*) Mean-square relative velocity of the particles in zero gravity, in the gravity direction (z). A, corn; B, solid glass; C, copper.

6.1. *Mean-square relative velocity*

The mean-square relative velocity in the x_i-direction is a measure of the deviation of the particle velocity fluctuation from that of the surrounding fluid, and is defined as:

$$\langle v^2_{i,\mathrm{rel}}(t) \rangle = \langle \{v_i(\boldsymbol{r},t) - u_i[\boldsymbol{x}(\boldsymbol{r},t),t]\}^2 \rangle, \tag{15}$$

where $\boldsymbol{r}$ is the injection position of the solid particle, and $\boldsymbol{x}$ is its current position, i.e. $\boldsymbol{x}_{\mathrm{inj}} = \boldsymbol{x}(\boldsymbol{r}, t_{\mathrm{inj}})$. As was mentioned in §4, the particles are injected at dimensionless time $T = 2$ which equals t_{inj}.

The temporal behaviour of $\langle v^2_{i,\mathrm{rel}} \rangle$ is used to determine the time at which the particles become independent of their injection conditions. Riley & Patterson (1974) were the first to use the time of occurrence of the peak of $\langle v^2_{i,\mathrm{rel}} \rangle$ to indicate the time at which the particles had adjusted to the decaying turbulence.

Figure 8(*a*) shows the time development of $\langle v^2_{1,\mathrm{rel}} \rangle$ for the three particles (A: corn, B: glass, C: copper) under gravity and zero-gravity conditions. It should be noted that the time axis t in figure 8 is dimensionless and is measured from t_{inj}, and thus $t = 0$ *in* these figures correspond to $T = 2$. Throughout the remainder of the paper the time origin, t_0, of all the statistical quantities of a particle is the time of the peak of its $\langle v^2_{i,\mathrm{rel}} \rangle$, or t_{peak}.

The development of $\langle v^2_{2,\mathrm{rel}} \rangle$ (not shown) is nearly identical to that of $\langle v^2_{1,\mathrm{rel}} \rangle$ as expected in an isotropic flow. At zero time, $\langle v^2_{1,\mathrm{rel}} \rangle$ is zero according to the imposed initial condition of equal velocity of fluid and particle at injection. It is seen that particles with larger τ_{p}, hence higher inertia, have higher relative velocity in both

Particle	$\tau_{p,0}/\tau_{f,0}$	$(t_{peak}/\tau_{p,0})$ gravity	$(t_{peak}/\tau_{p,0})$ zero-gravity	$(t_{peak}/t_{v_t,max})$
Corn	0.09	2.61	1.96	0.40
Glass	0.203	1.16	1.45	0.24
Copper	0.221	1.07	1.33	0.14

TABLE 2. Time required by the particle to reach the peak of $\langle v_{1,rel}^2 \rangle$

conditions of gravity and zero gravity, owing to the smaller rate of decay of their kinetic energy compared to that of their surrounding fluid turbulence. However, if t_{peak} is normalized by $\tau_{p,0}$, we see in table 2 that the lighter the particle, the larger is $(t_{peak}/\tau_{p,0})$.

It is interesting to note that the values of $\langle v_{1,rel}^2 \rangle$ for the three particles in zero gravity become vanishingly small at $t = 5.5$, whereas they remain much higher for the particles in gravity. As will be discussed in the following sections, smaller values of $\langle v_{1,rel}^2 \rangle$ at large times correspond to higher velocity autocorrelations and higher turbulent diffusivity. On the other hand, gravity reduces particle velocity in the lateral directions, resulting in higher relative velocity between the particles and their surrounding fluid.

The time t_{peak} is also sensitive to the effects of inertia and gravity. In zero gravity, particles with higher τ_p need longer time to 'lose memory' of their initial velocity, hence their larger t_{peak} in figure 8(*a*). Gravity reduces particle velocity in the lateral directions, but in order to determine whether t_{peak} is reduced or increased we need to know the time $t_{v_t,max}$ at which the terminal velocity, v_t, attains its maximum value. This can be seen in figure 8(*b*) which shows the time development of $\langle v_{3,rel}^2 \rangle$ in the gravity direction (z), and clearly distinguishes the particle behaviour in that direction from that in the two lateral directions. It is clear that $\langle v_{3,rel}^2 \rangle$ increases until the particle reaches a steady free-fall velocity and then remains invariant. Having higher τ_p, the glass and copper particles have a larger $t_{v_t,max}$ than the corn particle. Therefore, the effect of the initial inertia of the corn particle is damped by gravity earlier than the heavier particles. This damping delays the occurrence of its relative velocity peak, hence an increased t_{peak} in gravity. On the other hand, t_{peak} of the heavier particles is reduced in gravity because their $t_{v_t,max}$ is much higher than their t_{peak} as shown in table 2. During this initial period, a heavy particle is more influenced by its inertia than by gravity (Yudine 1959) as will be discussed later.

In zero-gravity, figure 8(*c*) shows that $\langle v_{3,rel}^2 \rangle$ behaves in a very similar manner to that of $\langle v_{1,rel}^2 \rangle$ and $\langle v_{2,rel}^2 \rangle$. The effect of continuity and crossing trajectories is evidenced by comparing the zero-gravity distributions (dashed curves) of $\langle v_{1,rel}^2 \rangle$ (figure 8*a*) with their counterparts in the gravity case (solid curves). The maximum values of the three zero gravity curves are about 0.24–0.29 of the corresponding values in the gravity case. This means that continuity and crossing trajectories effects are the source of 76 % of $\langle v_{1,rel}^2 \rangle$ for the copper particle, and 71 % for the corn particle. In other words, for the particles studied here for which $(v_t/u_i) > 1$, and for long dispersion times, it is gravity, not inertia, that contributes most to the velocity difference between the particles and surrounding fluid. This is true in the lateral directions as well as in the gravity direction, though the gravity effect is more pronounced in the latter as expected (figure 8*b*, *c*).

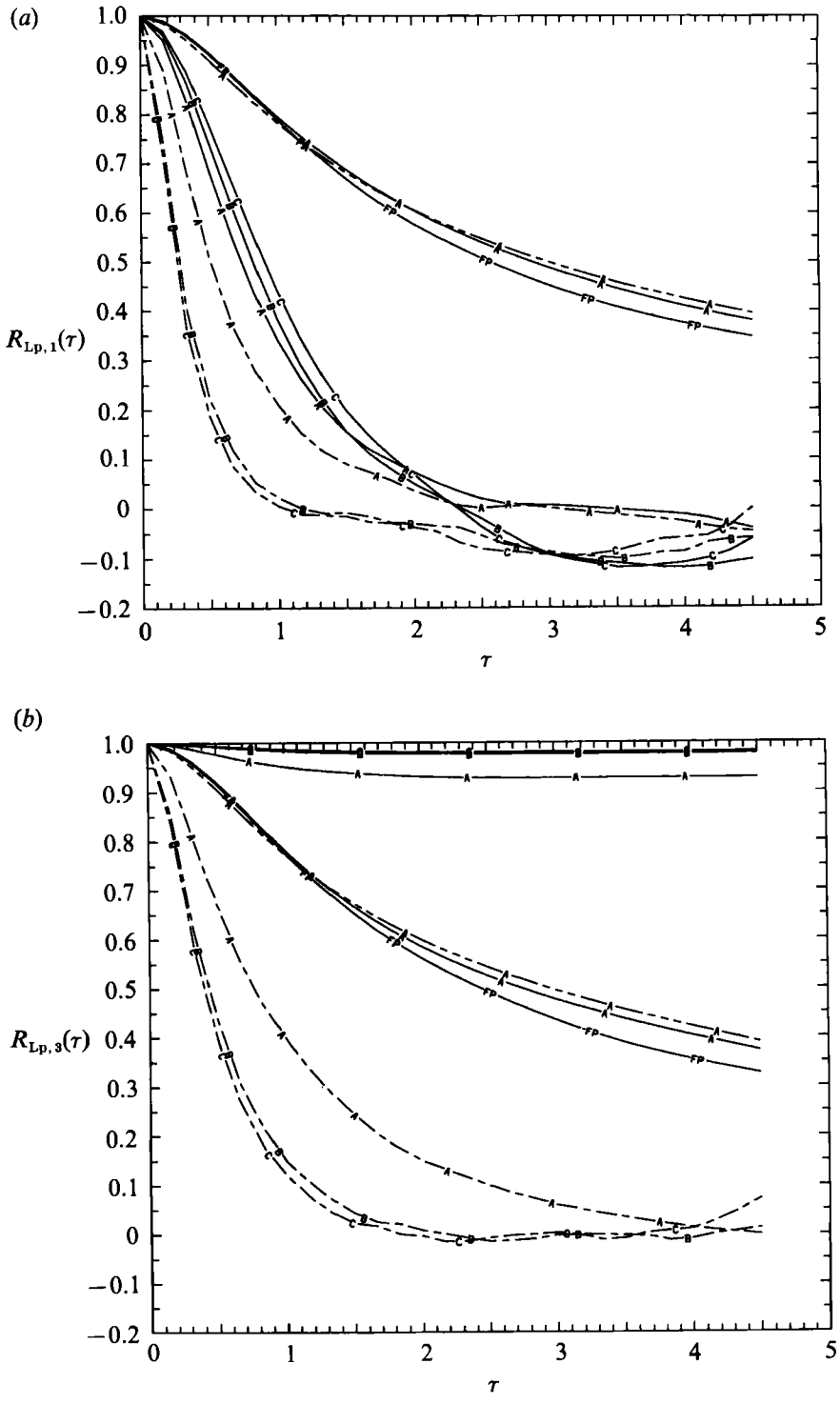

FIGURE 9(*a*,*b*). For caption see p. 673.

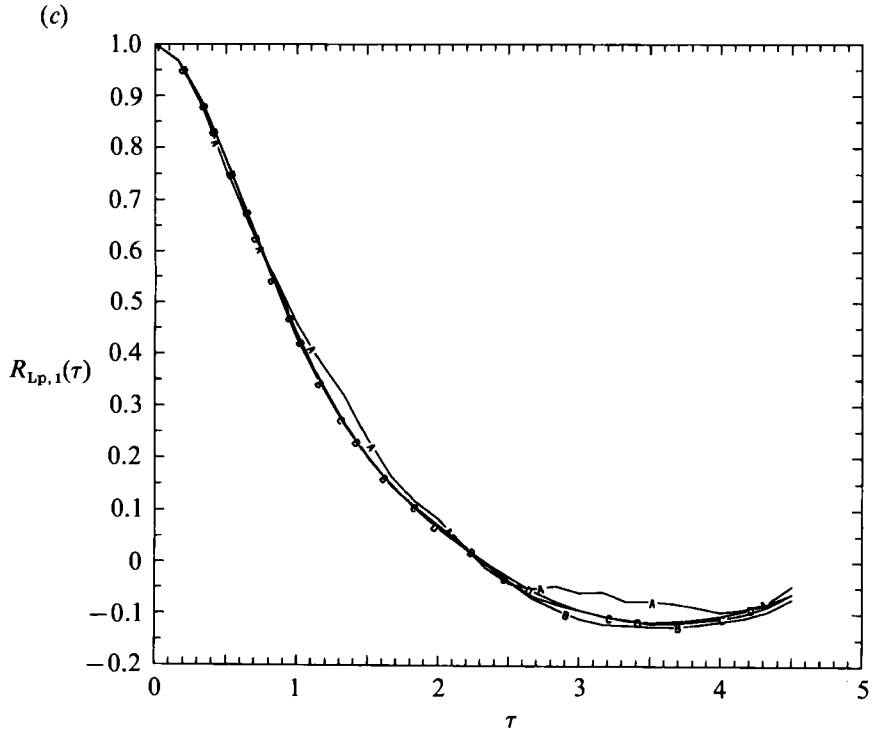

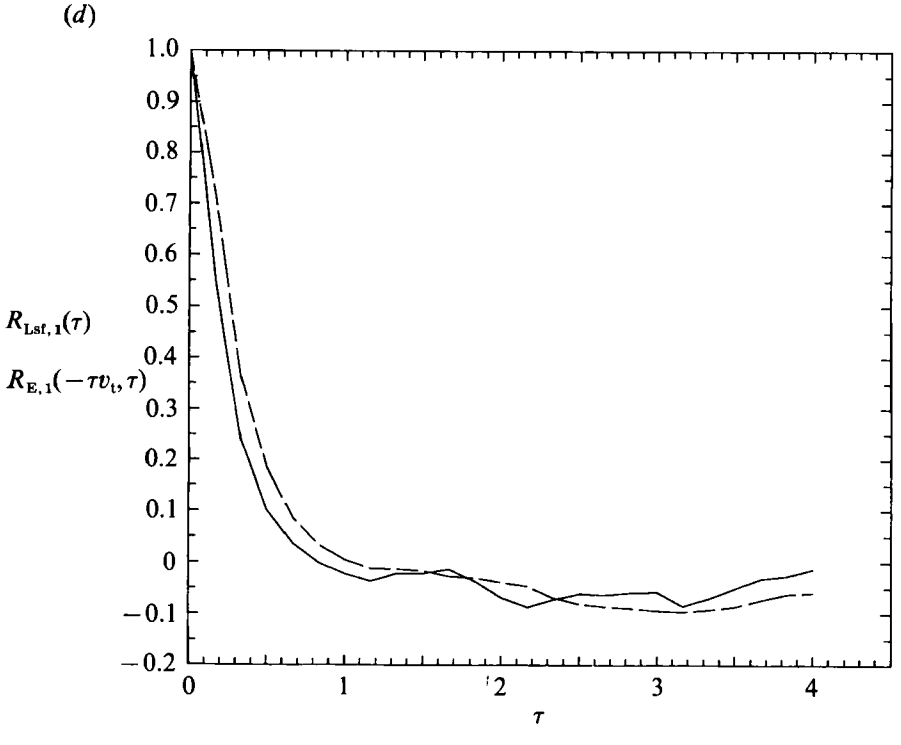

FIGURE 9(c, d). For caption see facing page.

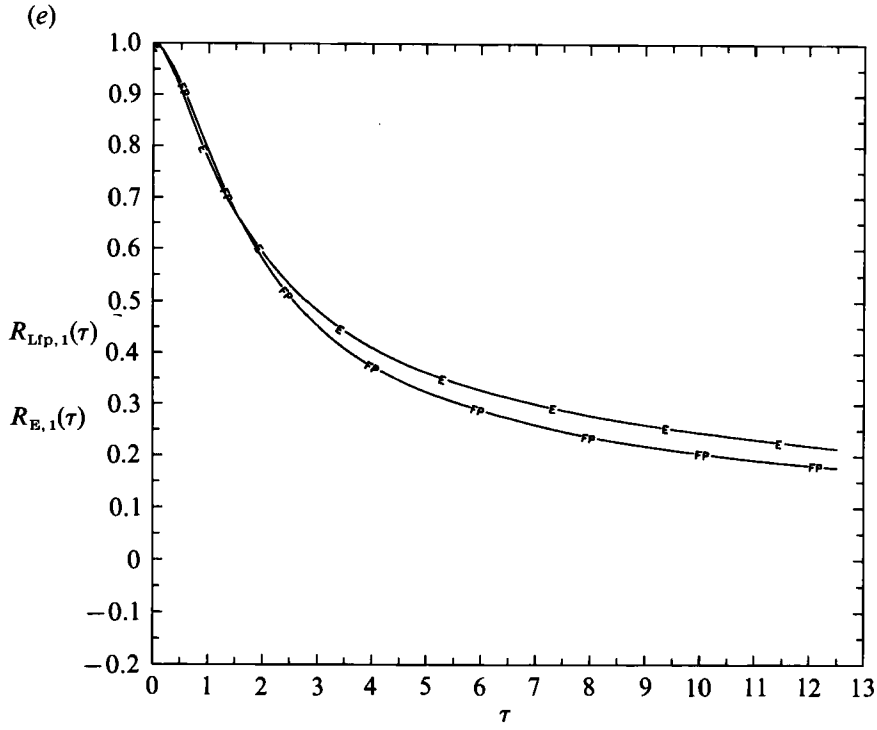

FIGURE 9. (*a*) Lagrangian velocity autocorrelations of the particles and their surrounding fluid in the lateral direction (x). (*b*) Lagrangian velocity autocorrelations of the particles and their surrounding fluid in the gravity direction (z). A, corn; B, solid glass; C, copper; FP, fluid point; ——, particles in gravity or zero gravity; – – – – –, surrounding fluid for particles in zero gravity; — — —, surrounding fluid for particles in gravity. (*c*) Lagrangian velocity autocorrelations of the copper particle in the lateral direction (x) in gravity. A, 8^3 particles; B, 16^3 particles; C, 22^3 particles; D, 32^3 particles. (*d*) Comparison between the Lagrangian velocity autocorrelation $R_{\mathrm{Lsf},1}$, (equation (22)), of the surrounding fluid of the copper particle in the lateral direction (x) (dashed line) and the instantaneous Eulerian spatial velocity correlation $R_{\mathrm{E},1}(-\tau v_{\mathrm{t}},\tau)$, (equation (23)), (solid line). (*e*) Comparison between $R_{\mathrm{E},1}(\tau)$, the one-point Eulerian fluid velocity correlation (E), and $R_{\mathrm{Lfp},1}(\tau)$, the Lagrangian autocorrelation of a fluid point (FP).

6.2. *Lagrangian velocity autocorrelation*

The Lagrangian autocorrelation coefficient, $R_{\mathrm{Lp},i}(t)$, of the particle velocity is defined as:

$$R_{\mathrm{Lp},i}(\tau) = \frac{\langle v_i(t_0)\, v_i(t_0+\tau)\rangle}{[\langle v_i^2(t_0)\rangle]^{\frac{1}{2}}[\langle v_i^2(t_0+\tau)\rangle]^{\frac{1}{2}}}, \tag{16}$$

with no summation on i, $i = 1, 2, 3$, and t_0 is the time at which we start computing the Lagrangian statistics (t_{peak} in table 2). Now if the turbulence is non-stationary, as in the decaying turbulence considered here, then the value of $R_{\mathrm{Lp},i}$ depends on the choice of t_0. SL used a time-coordinate stretching to transform the decaying field into a nearly stationary one. In the initial period of decay the energy $E \sim x^{-1}$, $u \sim x^{-\frac{1}{2}}$, and $l \sim x^{\frac{1}{2}}$, and thus $t \sim x$. SL divided the observed velocity fluctuations of the particle by the r.m.s. velocity of the particle at a selected measuring station ($x/M = 73$), and compensated for the increasing lengthscale, l, by dividing the separation distances by the distance from that reference station to the virtual origin. However, this decay correction implies the unjustified assumption that the particle

Particle	$T_{L,x}/\tau_{p,0}$(DNS)	$T_{L,x}/\tau_{f,0}$(DNS)	$T_{L,y}/\tau_{f,0}$(DNS)
Corn	3.814	0.344	0.351
Glass	1.741	0.354	0.365
Copper	1.721	0.381	0.396

TABLE 3. Particle Lagrangian integral timescale

velocity fluctuations decay at a rate equal to that of fluid turbulence. Here, the velocity autocorrelations are presented without scale stretching. As discussed in the preceding section, the starting time, t_0, in (16), is selected to coincide with t_{peak}. This method requires that two computer runs be performed for each of the three particles studied. The first run calculates the velocity and trajectory of a particle, its corresponding fluid point and surrounding fluid, and determines t_{peak}. The second run calculates the Lagrangian statistics starting from t_{peak}.

The autocorrelation coefficients for the solid particles and their surrounding fluid are shown in figure 9(*a*, *b*). In addition, the zero-gravity autocorrelations for the corn particle, its surrounding fluid, and its corresponding fluid point are shown (the three curves with highest magnitudes in figure 9*a*, *b*) for comparison.

The velocity autocorrelation coefficient for the fluid point is defined as:

$$R_{\mathrm{Lfp},i}(\tau) = \frac{\langle u_i(t_0)\, u_i(t_0+\tau)\rangle}{[\langle u_i^2(t_0)\rangle]^{\frac{1}{2}}[\langle u_i^2(t_0+\tau)\rangle]^{\frac{1}{2}}}. \tag{17}$$

The velocity autocorrelation coefficient for the fluid surrounding the particle is:

$$R_{\mathrm{Lsf},i}(\tau) = \frac{\langle u_i[x_{\mathrm{p},i}(t_0), t_0]\, u_i[x_{\mathrm{p},i}(t_0+\tau), (t_0+\tau)]\rangle}{\{\langle u_i^2[x_{\mathrm{p},i}(t_0), t_0]\rangle\}^{\frac{1}{2}}\{\langle u_i^2[x_{\mathrm{p},i}(t_0+\tau), (t_0+\tau)]\rangle\}^{\frac{1}{2}}}. \tag{18}$$

The crossing trajectories effects are readily seen for the corn particle by comparing its autocorrelations with and without gravity. In the gravity case, as the particle falls from its original location within a highly correlated velocity region and passes through various neighbouring vortical structures its memory of the original velocity decays much faster than in the zero-gravity case.

Now we compare the velocity autocorrelations of the three particles in the gravity case. It is seen that in the initial period where the effects of particle inertia dominate (see figure 8*b*), that $R_{\mathrm{Lp},1}$ of the heaviest particle (C) is higher than that of (A) for $\tau \leqslant 1.95$ (see table 1 for the value of the reference time used in normalizing τ). Similarly, $R_{\mathrm{Lp},1}$ of the glass particle (B) is higher than that of (A) for $\tau \leqslant 1.5$. For larger values of τ, the effects of gravity dominate, causing $R_{\mathrm{Lp},1}$ of the heavier particles to decay faster, vanish and become negative at earlier times than that of the lighter particle. The negative part of $R_{\mathrm{Lp},1}$ will be discussed later. A rough measure of the time interval over which $v_i(t)$ is correlated with itself is the Lagrangian integral timescale, defined as

$$T_{L,i} = \int_0^\infty R_{\mathrm{Lp},i}(t)\,\mathrm{d}t. \tag{19}$$

Table 3 shows the computed Lagrangian integral timescales, normalized by $\tau_{f,0}$, for the two lateral directions. We see that the Lagrangian timescale is highest for the particle with highest τ_p (copper) and smallest for the corn particle. In other words the

effects of inertia in the initial period (figure 9*a*) contribute more to the integral in (19) than the effects of gravity. It should be noted that the maximum lag time, $\tau = 4.5$, used in (16) to compute $R_{\mathrm{Lp},i}(\tau)$ equals respectively 4.6, 4.5, and 4.2 times the Lagrangian integral timescale, $T_{\mathrm{L},x}$, for the corn, glass, and copper particles. $T_{\mathrm{L},x}$, in turn, ranges from about 3.8 to 1.7 times $\tau_{\mathrm{p},0}$ of these particles (table 3). This indicates that sufficient time has elapsed for the particles to lose the 'memory' of their conditions at time t_0, and dispersion then is classified as 'long-time dispersion'. Thus, continuing the computation beyond this time would not provide additional statistical information of interest.

It should be mentioned that $R_{\mathrm{Lp},1}$ (figure 9*a*) starts to deviate from $R_{\mathrm{Lp},2}$ (not shown) after both decay to zero. The former assumes larger negative values than the latter, i.e. $R_{\mathrm{Lp},1}$ displays a much larger 'negative loop' than $R_{\mathrm{Lp},2}$ does. The negative loops are due to the continuity effect discussed below, and the difference in their size is due only to the increased anisotropy of the carrier fluid (figure 4) as a result of turbulence decay and increased length scales. Figure 4 shows that B_{11} is positive during this period, whereas B_{22} is smaller and negative, i.e. $\langle u_1^2\rangle > \langle u_2^2\rangle$.

Csanady (1963) examined the conditions under which negative loops occur in the particle Lagrangian autocorrelations. He postulated that if the terminal velocity is sufficiently high then there must exist negative portions of the Lagrangian lateral autocorrelations because continuity requires that the space–time correlations or delayed-time Eulerian correlations, $R_{\mathrm{E},i}$ satisfy the following relationships (Townsend 1976)

$$\int_{-\infty}^{\infty}\int_{-\infty}^{\infty} R_{\mathrm{E},2}\,\mathrm{d}x_1\,\mathrm{d}x_3 = 0, \tag{20}$$

$$\int_{-\infty}^{\infty}\int_{-\infty}^{\infty} R_{\mathrm{E},1}\,\mathrm{d}x_2\,\mathrm{d}x_3 = 0. \tag{21}$$

Accordingly, Csanady labelled the occurrence of the negative loops as 'continuity effect' which is a consequence of the 'crossing trajectories effect'. And both effects reduce the dispersion of solid particles in the directions normal to that of gravity.

Csanady (1963) also explained the similarity between $R_{\mathrm{Lsf},1}$ and $R_{\mathrm{E},1}$ as follows. When a particle with high terminal velocity crosses an eddy, in the x_3- or gravity-direction, the lateral turbulent dispersion can be neglected as compared to the distance travelled, i.e. $\langle x_{\mathrm{p},1}^2\rangle^{\frac{1}{2}} \ll |\tau v_{\mathrm{t}}|$. Thus during the fall time τ we have

$$R_{\mathrm{Lsf},1} = \frac{\langle u_1[x_{\mathrm{p},3}(t_0), t_0]\, u_1[x_{\mathrm{p},3}(t_0+\tau), (t_0+\tau)]\rangle}{\{\langle u_1^2[x_{\mathrm{p},3}(t_0), t_0]\rangle\}^{\frac{1}{2}}\{u_1^2[x_{\mathrm{p},3}(t_0+\tau), (t_0+\tau)]\rangle\}^{\frac{1}{2}}}, \tag{22}$$

$$R_{\mathrm{E},1}(-\tau v_{\mathrm{t}}, \tau) = \frac{\langle u_1(x_3, t_0)\, u_1((x_3-\tau v_{\mathrm{t}}), (t_0+\tau))\rangle}{[\langle u_1^2(x_3, t_0)\rangle]^{\frac{1}{2}}[\langle u_1^2((x_3-\tau v_{\mathrm{t}}), (t_0+\tau))\rangle]^{\frac{1}{2}}}. \tag{23}$$

Now for a particle with a high terminal velocity, the fall time τ may be neglected compared to the eddy turnover time (see (13)), or equivalently the change in the eddy size during the time τ can be neglected compared to the spatial change of $R_{\mathrm{E},1}$. Thus $R_{\mathrm{E},1}$ becomes the instantaneous spatial velocity correlation at two points separated by the vertical distance τv_{t}, and thus $R_{\mathrm{Lsf},1}$ approaches $R_{\mathrm{E},1}$. Figure 9(*d*) compares $R_{\mathrm{Lsf},1}(\tau)$ of the copper particle with the instantaneous Eulerian spatial correlations of the fluid velocity $R_{\mathrm{E},1}(-\tau v_{\mathrm{t}}, \tau)$. The figure shows that the two correlations are quite similar but not identical. This is expected, since the copper particle is not falling in an exactly vertical direction (see figure 10*c*, *d*), and thus $R_{\mathrm{Lsf},1}$ should be

slightly higher than $R_{E,1}$ for the initial period $\tau \leqslant 2.4$. A much heavier particle would be needed for the two correlations to be identical. Csanady showed that this similarity is valid if $|v_t| \geqslant 4\langle u_3^2\rangle^{\frac{1}{2}}$. This condition is satisfied for the glass and copper particles but not for the corn particle, hence the negative loops in $R_{Lp,1}$ of the glass and copper particles. More supporting evidence is presented later in §6.3.

Also shown in figure 9(*a*) are the velocity autocorrelations of the surrounding fluid, $R_{Lsf,1}(\tau)$, for each of the three particles in the gravity case. As expected, these autocorrelations decay much faster than those of the corresponding solid particles. A solid particle retains, to some extent, information of its velocity at earlier times. The 'host fluid' surrounding the particle at time t, on the other hand, has little information about the velocity of the earlier host fluid at time $(t-\tau)$, and this little information diminishes further as the particle migrates to yet another host, especially in a decaying turbulence.

It is interesting to note that owing to the inertia of the corn particle, its $R_{Lp,1}$ in zero-gravity is higher than that of the corresponding fluid point. The same is true for the other two particles (not shown). More interesting is that $R_{Lsf,1}$ of the fluid surrounding the corn particle in zero-gravity is higher than that of the particle itself for $\tau > 2$, i.e. a behaviour opposite to that in gravity environment. In the absence of gravity the solid particle stays longer in an eddy before it crosses it to another, and the fluid velocity in an eddy is more correlated with itself than the particle velocity is. In the initial period, $\tau < 2$, where the particle inertia dominates the reverse behaviour is seen.

Figure 9(*b*) shows $R_{Lp,3}$ for the three particles with gravity (the three curves with highest magnitudes) and their surrounding fluid, $R_{Lsf,3}$ (the three curves with lowest magnitudes). Also shown is $R_{Lp,3}$ for the corn particle in zero gravity, its corresponding fluid point, and its surrounding fluid. Again the behaviour of the autocorrelations in the gravity direction, as expected, is significantly different from that in the two lateral directions. The nearly invariant terminal velocity, v_t (see figure 8*b*), during most of the period of calculating $R_{Lp,3}$, and the fact that $(v_t/u_3) > 1$ result in the depicted asymptotic behaviour of $R_{Lp,3}$. Once gravity is eliminated, then $R_{Lp,3}$ duplicates the developments of $R_{Lp,1}$ and $R_{Lp,2}$ as shown for the corn particle and its surrounding fluid. Of course $R_{Lfp,3}$ of the fluid point is independent of gravity and is nearly identical to its counterparts in the lateral directions.

It was mentioned earlier in §3 that we used 22^3 particles for our simulation based on a comparison between the results of 8^3, 16^3, 22^3 and 32^3 particles. Figure 9(*c*) shows this comparison for $R_{Lp,1}(\tau)$ of the copper particle using 8^3, 16^3, 22^3 and 32^3 particles, denoted respectively by A, B, C and D. It is seen that curves C and D nearly coincide throughout the computation period, whereas that corresponding to the smallest number of particles (A) deviates from them. Based on this comparison and a similar one in the next section we decided that the statistics obtained from 22^3 particles are sufficiently accurate.

Finally, a comparison between the one-point Eulerian fluid velocity correlation $R_{E,1}(\tau)$ and the Lagrangian autocorrelation of a fluid point $R_{Lfp,1}(\tau)$ is shown in figure 9(*e*). The one-point Eulerian correlation is defined as:

$$R_{E,i}(\tau) = \frac{\langle u_i(x_i, t_0)\, u_i(x_i, t_0+\tau)\rangle}{[\langle u_i^2(x_i, t_0)\rangle]^{\frac{1}{2}}[\langle u_i^2(x_i, t_0+\tau)\rangle]^{\frac{1}{2}}}. \tag{24}$$

The figure shows that the present results are qualitatively similar to those of Riley & Patterson (1974). For small values of τ ($\tau \leqslant 1.5$, i.e. $(\tau/\tau_{f,0}) \leqslant 0.5$), we see that

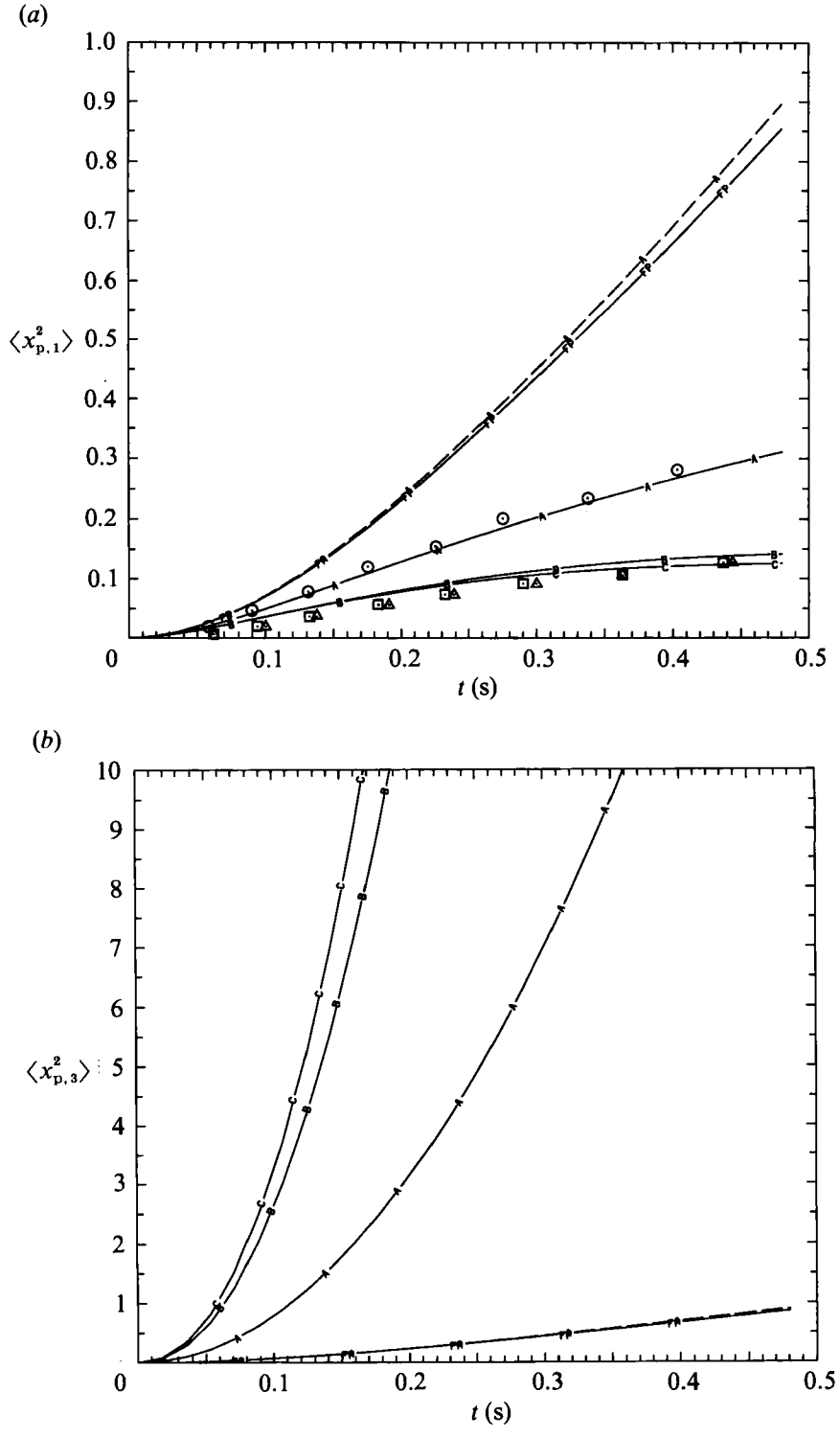

FIGURE 10(*a*, *b*). For caption see p. 680.

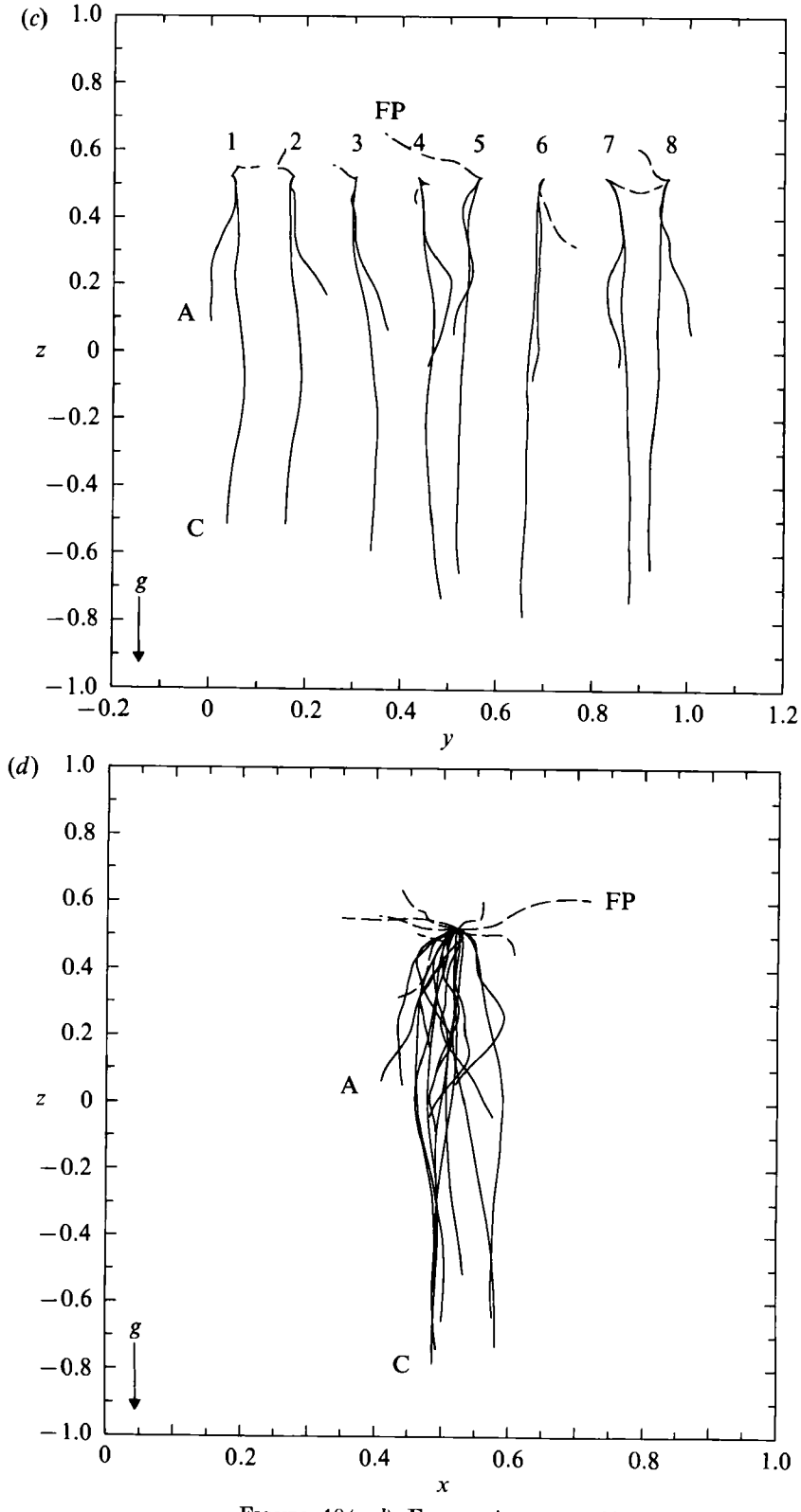

FIGURE 10(c, d). For caption see p. 680.

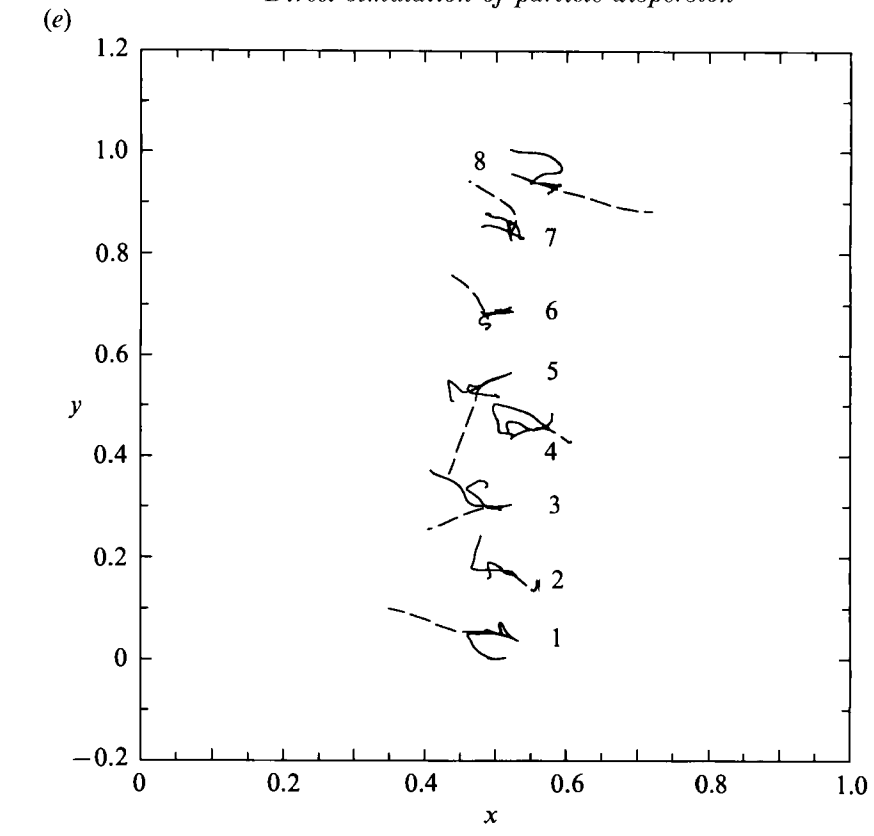

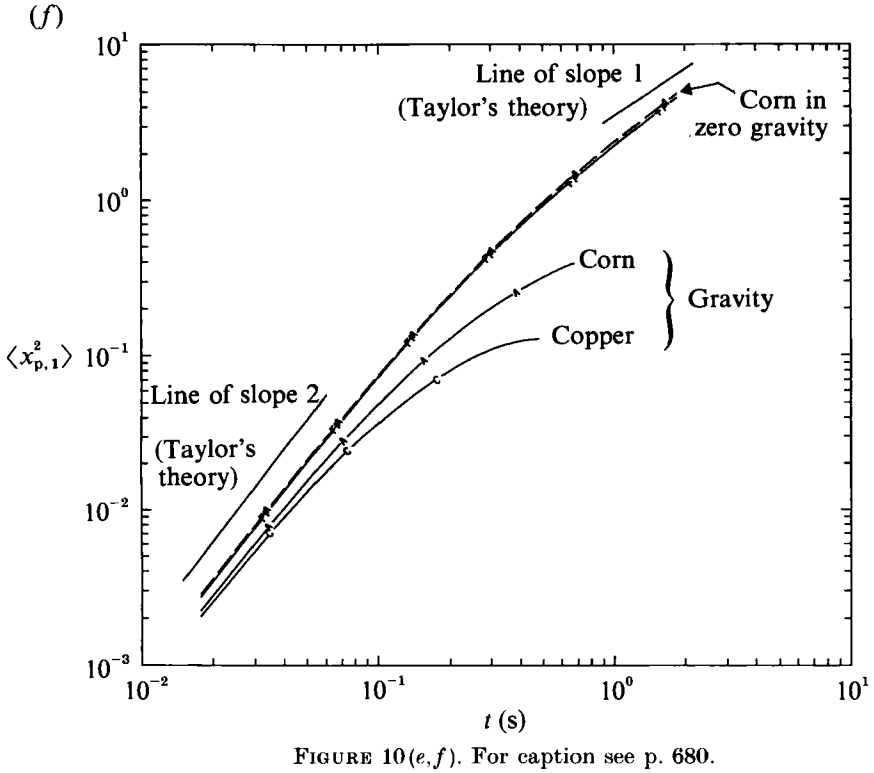

FIGURE 10(*e*,*f*). For caption see p. 680.

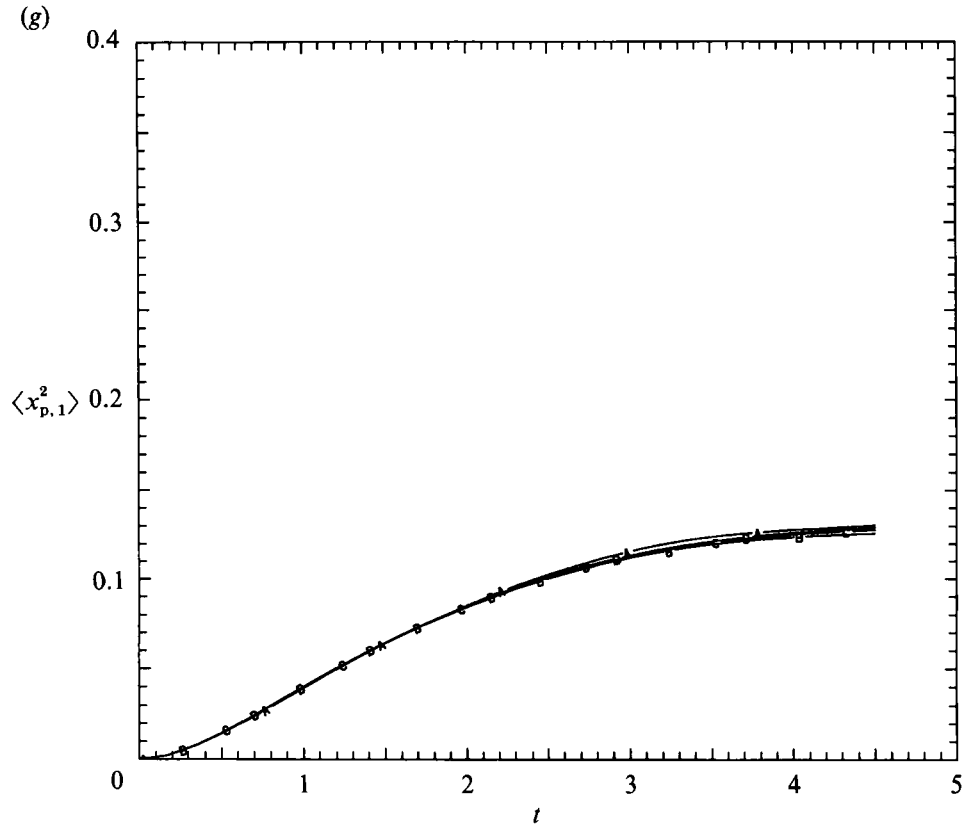

FIGURE 10. (*a*) Normalized mean-square displacement in the lateral direction (x). FP, fluid point; A, corn; B, solid glass; C, copper; ——, in gravity; — —, zero gravity. Snyder & Lumley: ⊙, corn; □, solid glass; △, copper. (*b*) Normalized mean-square displacement in the gravity direction (z). (*c*) Trajectories of eight particles in gravity and eight fluid points projected onto a vertical (y, z)-plane. (*d*) Trajectories of eight particles in gravity and eight fluid points projected onto a vertical (x, z)-plane. (*e*) Trajectories of eight particles in gravity and eight fluid points projected onto a horizontal (x, y)-plane. (*f*) Comparison of the normalized mean-square displacement in the lateral direction (x) with Taylor's theory for short time (line of slope 2) and long time (line of slope 1) dispersion. (*g*) Normalized mean-square displacement in gravity of the copper particle in the lateral direction (x). A, 8^3 particles; B, 16^3 particles; C, 22^3 particles; D, 32^3 particles.

$R_{\mathrm{Lfp},1}(\tau)$ is slightly larger than $R_{\mathrm{E},1}(\tau)$, and that this trend is reversed for larger τ. The recent study of Kaneda & Gotoh (1991) for decaying isotropic turbulence supports our results for small τ. However, our results show that the differences between $R_{\mathrm{Lfp},1}(\tau)$ and $R_{\mathrm{E},1}(\tau)$ are small relative to the magnitude of either correlation. This supports the assumption that $R_{\mathrm{Lfp},1}(\tau) \approx R_{\mathrm{E},1}(\tau)$ in nearly isotropic turbulence. Shlien & Corrsin (1974), though their experiment showed larger difference between the two correlations for small τ, indicated that it is possible that $R_{\mathrm{Lfp},1}(\tau) > R_{\mathrm{E},1}(\tau)$ for large τ.

6.3. *Mean-square displacement*

The mean-square displacement (dispersion) of a solid or fluid particle in the x_i-direction is calculated from:

$$\langle x^2_{\mathrm{p},i}(t) \rangle = \frac{1}{N} \sum_{j=1}^{N} [x_{\mathrm{p},i}(t) - x_{\mathrm{p},i}(t_0)]^2_j, \tag{25}$$

where N is the total number of particles and t_0 equals t_{peak}, the time at which $\langle v^2_{i,rel}\rangle$ peaks.

Since the turbulence energy and lengthscales in the simulation differ from those in the experiment of SL, as mentioned in §5, the mean square displacement, $\langle x^2_{p,i}(t)\rangle$, of the particles must be appropriately normalized before comparing the DNS results with those of SL. Here we normalize $\langle x^2_{p,i}(t)\rangle$ by l_0^2, where l_0 is the integral lengthscale (see (14)) at t_{peak}.

Figure 10(*a*) compares the numerical and experimental time development of $\langle x^2_{p,1}(t)\rangle$ for the three particles. As expected, the lighter particle, with smaller τ_p, disperses laterally more than the heavier particles. The agreement between the computed and experimental values is good for the corn particle throughout the entire range of SL's data. However, the simulation of the glass and copper particles overestimates $\langle x^2_{p,1}(t)\rangle$ in the initial period, while the agreement improves as the long-time dispersion regime is approached. There are two possible reasons for the overestimation during the initial period. First, there is uncertainty about matching the starting time t_0 of computing $\langle x^2_{p,1}(t)\rangle$ in the simulation with that of the experiment, even though the decay rates of turbulence energy in both are in very good agreement. As was mentioned in §6.1, we assume that the starting time coincides with that of the peak of $\langle v^2_{1,rel}(t)\rangle$ (figure 8*a*), but the experiment of SL did not provide information about the time development of $\langle v^2_{1,rel}(t)\rangle$. Secondly, we normalize $\langle x^2_{p,1}(t)\rangle$ by the square of the integral lengthscale l_0 at the time of that peak. Therefore, one or both of these factors would lead to the disagreement in figure 10(*a*). The simulation and experiment both indicate that the mean-square displacement of the glass particle is higher than that of the copper particle. However, the difference between the $\langle x^2_{p,1}(t)\rangle$ curves of the two particles is slightly higher in the simulation than in the experiment.

Also shown in figure 10(*a*) is the time development of $\langle x^2_{p,1}\rangle$ of a corn particle in zero gravity and of the corresponding fluid point. The effect of gravity in reducing particle dispersion in the lateral directions is evident in the figure. For example, at time $t = 0.4$ s $\approx 3.85T_{L,x}$, we see that $\langle x^2_{p,1}\rangle$ of the corn particle is only 40% of its zero-gravity value. It is also seen that in zero-gravity, the corn particle disperses in the lateral directions slightly more than the corresponding fluid point. This is in accordance with the behaviour of their respective autocorrelations which was explained in §6.2.

The time development of $\langle x^2_{p,3}\rangle$ of the three particles is shown in figure 10(*b*) together with that of the corn particle in zero gravity and its corresponding fluid point. As expected, we see that the magnitudes of $\langle x^2_{p,3}\rangle$ for the three particles are now in reverse order to that in the lateral directions, i.e. $\langle x^2_{p,3}\rangle$ is highest for the copper particle, followed by the glass particle and is lowest for the corn particle. This behaviour agrees with that of $R_{Lp,3}$ in figure 9(*b*) and that of $\langle v^2_{rel,3}\rangle$ in figure 8(*b*).

It should be noted that the $\langle x^2_{p,3}(t)\rangle$ curves of the three solid particles continue to be parabolic even after long dispersion times, i.e. they follow a t^2 behaviour in contrast to that of $\langle x^2_{p,1}\rangle$ (figure 10*a*). This is due to the effect of terminal velocity, v_t, which acts as an imposed, nearly constant, mean velocity with a magnitude higher than that of $u_{3,rms}$. Consequently, $R_{Lp,3}$ attains a nearly constant value close to unity (figure 9*b*) as explained earlier in §6.2. Now following Taylor's (1921) approach, it is easy to show that $\langle x^2_{p,3}(t)\rangle \sim t^2$. Further evidence will be presented in §6.4.

It should be stressed here that the large magnitudes of $\langle x^2_{p,3}(t)\rangle$ relative to those of $\langle x^2_{p,1}(t)\rangle$ are a direct result of the large relative magnitudes of the instantaneous velocity of the particle in the x_3-direction. This velocity component, v_3, in turn

consists of a mean drift velocity and a small fluctuating turbulent velocity, the former being an order of magnitude larger than the latter (figure 8*b*, *c*). Thus, in a gravity environment only the mean-square displacements in the lateral directions, $\langle x^2_{p,1}(t)\rangle$ and $\langle x^2_{p,2}(t)\rangle$, represent a true measure of *turbulent dispersion* since there is no mean drift in these two directions.

An even clearer picture of particle dispersion anisotropy in the three directions is displayed in figure 10(*c*, *d*, *e*). The three figures show the projections, on two vertical planes (yz, xz) and a horizontal plane (xy) respectively, of the instantaneous trajectories in gravity environment, during the same period of time, of 8 corn particles (A), 8 copper particles (C) and 8 fluid points (FP). Each set of 8 particles was selected from the total of 10648 particles whose trajectories are computed. At injection, the solid particles and fluid points exist along the horizontal line of intersection of the horizontal plane $z = 0.52$ and the vertical plane $x = 0.52$. The particles are equally spaced in the y-directions between $y = 0.04$ and $y = 0.96$.

Figure 10(*c*) shows the projected trajectories of the solid particles (solid lines) and fluid points (dashed lines) on the vertical plane (yz). The eight short lines are the trajectories of the corn particles, and the eight long lines are those of the copper particles. Figure 10(*d*) presents a side view of the same trajectories while figure 10(*e*) shows the view from the top.

It is seen that the fluid points disperse laterally in the x- and y-directions more than the corn particles, and these in turn disperse more than the copper particles. The local three-dimensional stretching and bending of a large eddy control the displacement of the fluid point which is an integral part of the fluid element. As a result, the eight fluid points do not exhibit any preferred direction of dispersion. The statistically isotropic dispersion obtained from the trajectories of all the 10648 fluid points is also evident by comparing the instantaneous displacement of the fluid points in figure 10(*c*, *d*, *e*). The solid particle, on the other hand, owing to its own inertia and the acceleration of gravity, cannot follow the fluid point but moves mainly downward in the gravity direction, while simultaneously responding to the lateral fluctuations caused by the local turbulence. It should be recalled here (from §§2 and 4) that our computation domain is moving with a constant mean stream velocity in the direction opposite to gravity. This means that in a wind tunnel (e.g. that of SL) all the particles will be advected upwards but the copper particles will always lag behind the corn particles or the fluid points.

As discussed earlier (§6.2), Csanady (1963) postulated that the particle velocity autocorrelation should have a negative loop if $\langle x^2_{p,1}\rangle^{\frac{1}{2}} \ll |\tau v_t|$. Figure 10(*c*, *d*) indicates that this condition is met for the copper but not for the corn particles, again in accord with the negative loop in $R_{Lp,1}$ for the copper particle in figure 9(*a*).

It is of interest to compare the computed time development of $\langle x^2_{p,1}(t)\rangle$ for both a solid particle and its corresponding fluid point with that obtained analytically by Taylor's theory (1921) of 'diffusion by continuous movements'. It should be noted that Taylor's theory was formulated for a fluid point in a stationary homogeneous turbulence. However, the stationarity condition can be relaxed owing to the self preservation property of turbulence during the initial period of decay. As discussed in §6.2, during this period the turbulence energy $E \sim x^{-1}$, $u \sim x^{-\frac{1}{2}}$, and $l \sim x^{\frac{1}{2}}$. Thus the turbulent diffusivity, $D_t \sim lu$, is independent of distance from the grid as in the case of stationary turbulence for times greater than the Lagrangian timescale. This self preservation property of grid turbulence allows the comparison of the computed $\langle x^2_{fp,1}(t)\rangle$ of a fluid point with that obtained by Taylor's theory.

Now, care is needed when applying this theory to the dispersion of a solid particle

in gravity environment. The theory requires that the velocity of the fluid point be random. This condition allows us to examine effectively the solid particle motion only in the plane perpendicular to the direction of gravity because gravity imposes a significant (non-random) force on the particle in the vertical direction. For example, if the ratio $v_t/u_0 \gg 1$ the particle will fall vertically downward without any appreciable randomness in velocity in that direction. Therefore we limit the following discussion to the dispersion of the fluid point and solid particle in the x_1- (or x_2-) direction.

The main result of Taylor's theory, relevant to our study, is that for a fluid point,

$$\langle x_i^2(T)\rangle = 2\langle u_i^2\rangle \int_0^T \int_0^t R_\tau \,\mathrm{d}\tau \,\mathrm{d}t,$$

where R_τ is the Lagrangian velocity correlation coefficient of the fluid point. More specifically, Taylor assumed that for 'long time' dispersion

$$\int_0^t R_\tau \,\mathrm{d}\tau = I,$$

where I is a finite value. This 'long time' is generally taken as ($t \geqslant 5T_{\mathrm{L},x}$) (Monin & Yaglom 1979). This leads to

$$\langle x_i^2(T)\rangle = 2\langle u_i^2\rangle IT,$$

$$\mathrm{d}/\mathrm{d}t\langle x_i^2(T)\rangle = 2\langle u_i^2\rangle I,$$

in stationary turbulence. Thus, for long times, $\langle x_i^2(T)\rangle$ of a fluid point varies linearly with time, and the turbulent diffusivity tends to be constant. For short times, Taylor showed that $\langle x_i^2(T)\rangle \sim T^2$, and thus $\mathrm{d}/\mathrm{d}t\langle x_i^2(T)\rangle \sim T$. Now, we examine our results to see whether the above relations apply to the lateral dispersion of a solid particle as well.

Figure 10(f) shows good agreement between $\langle x_{\mathrm{fp},1}^2(t)\rangle$ of the fluid point with the two theoretical asymptotic lines. The first line has a slope of 2 for the short-time dispersion, and second has a slope of 1 for the long-time dispersion. Nearly identical behaviour is displayed for the corn particle in zero gravity. In contrast, $\langle x_{\mathrm{p},1}^2(t)\rangle$ of the corn particle in gravity environment deviates, after a short time from the start, from that of Taylor's theory, and the deviation increases with time. As discussed in §6.1, at longer times the particle becomes more influenced by gravity than by its own inertia (Yudine 1959). Also displayed in figure 10(f) is $\langle x_{\mathrm{p},1}^2(t)\rangle$ of the copper particle with gravity, and as expected the deviation from the theoretical asymptotes is now far greater than that of the corn particle. Now, our computed Lagrangian velocity correlation coefficients for the solid particles show that $R_{\mathrm{Lp,1(grav)}} \ll R_{\mathrm{Lp,1(zero\,grav)}}$ (figure 9a) owing to the crossing trajectories effect. Furthermore, in gravity, the variance $\langle v_1^2\rangle$ of the solid particle decays faster than $\langle u_1^2\rangle$ of the fluid, as evident in the experiment of SL and our simulations (not shown). In addition, the decay rate of $\langle v_1^2\rangle$ is a nonlinear function of (v_t/u_0), and does not follow the established behaviour of $\langle u_i^2\rangle \sim t^{-1}$ of decaying turbulence. Therefore, whereas $\langle u_i^2\rangle$ was constant in Taylor's derivation for stationary turbulence, $\langle v_i^2\rangle$ of the solid particle in gravity cannot be, and thus the double time-integration should be made over the product $\langle v_i^2\rangle R_\tau$. Our simulations indicate that the time decay rate of the quantity $\langle v_1^2\rangle R_\tau$ for the particle produces a nearly constant $\langle x_{\mathrm{p},1}^2(T)\rangle$ for large T, and hence a vanishing $\mathrm{d}/\mathrm{d}t\langle x_{\mathrm{p},1}^2(T)\rangle$ (figures 10a and 11b). Note that these results cannot be

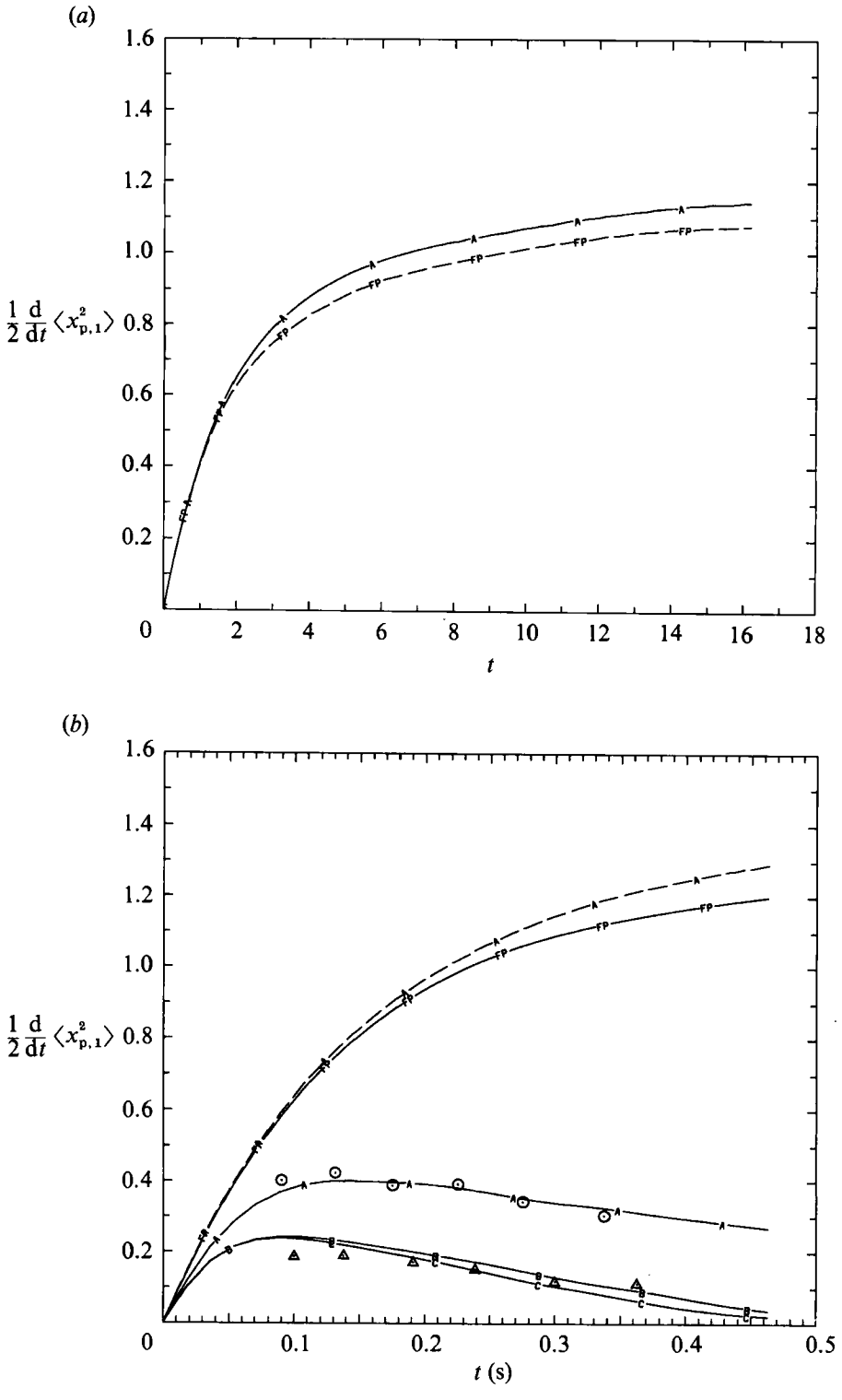

FIGURE 11 (*a*, *b*). For caption see facing page.

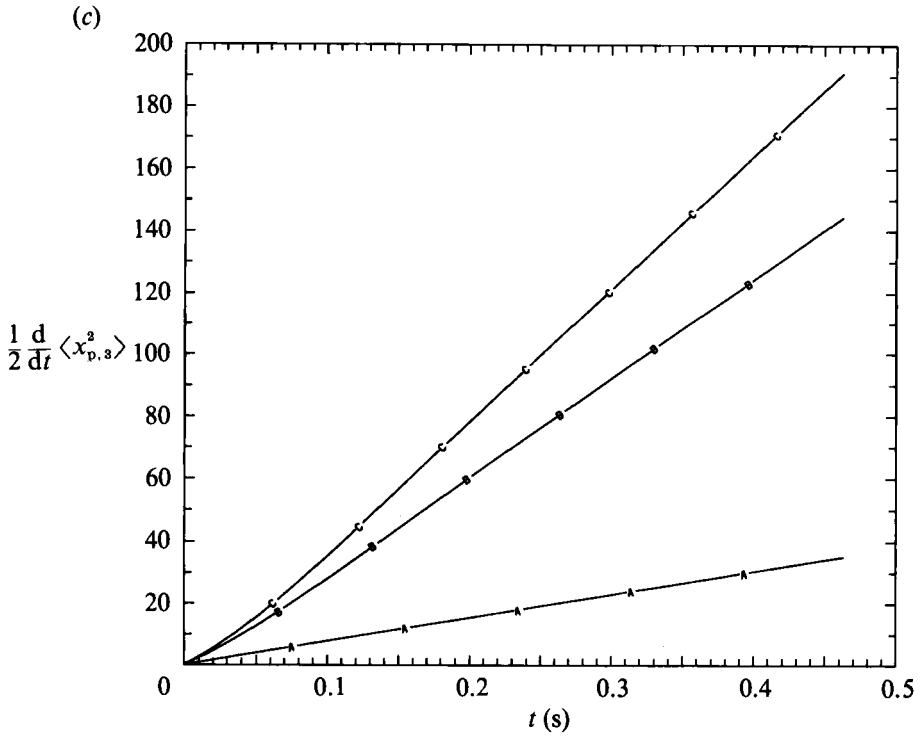

FIGURE 11. (*a*) Normalized turbulent diffusivities in the lateral direction (x) in zero gravity. A ——, corn; FP ——, fluid point. (*b*) Normalized turbulent diffusivities in the lateral direction (x). A, corn; B, solid glass; C, copper; FP, fluid point; ——, in gravity; — —, zero gravity. Snyder & Lumley: ⊙, corn, △, solid glass and copper. (*c*) Normalized turbulent diffusivities of the particles in gravity, in the gravity direction (z).

attributed to the non-stationarity of the decaying turbulence of the carrier fluid, since $\langle x_{p,1}^2(T)\rangle$ of the same particle in the same flow, but in zero gravity increases linearly with T (figure 10*a*, *f*).

In summary, gravity effects prevent $\langle x_{p,1}^2(T)\rangle$ of the solid particle from increasing linearly with time, and restrict it to a nearly constant value for long times. Consequently, the turbulent diffusivity of the particle in gravity approaches zero asymptotically (figure 11*b*).

The accuracy of computing the statistics of particle dispersion is demonstrated again by comparing the time development of $\langle x_{p,1}^2\rangle$ of the copper particle using 8^3, 16^3, 22^3 and 32^3 particles in figure 10(*g*) (denoted *A*, *B*, *C* and *D* respectively). Table 4 presents the percentage difference at $t = 4.5$ in the mean square displacement of the particle, $\langle x_{p,1}^2\rangle$, and $R_{Lp,1}(\tau)$ for the three realizations using 8^3, 16^3 and 22^3 particles with respect to a simulation using 32^3 particles. These tests were performed using the same Eulerian flow field. In addition, we have performed other tests, not reported here, using different Eulerian realizations. These were obtained using the same mesh, 96^3, and R_{λ_0} and the same number of particles, but varying the initial r.m.s. velocity, u_0^*, or the value of k_p/k_{min} in the initial spectrum $E(k, 0)$. Increasing u_0^* by 50%, or decreasing k_p/k_{min} from 6 to 4 (thus increasing l_0), resulted in less than 1% change in either $\langle x_{p,1}^2\rangle$ or $R_{Lp,1}$.

Number of particles	Difference in $\langle x^2_{\mathrm{p},1}\rangle$	Difference in $R_{\mathrm{Lp},1}$
8^3	2.0%	25%
16^3	1.0%	16%
22^3	0.89%	0.75%

TABLE 4. Percentage difference in the copper particle statistics at $t = 4.5$ with respect to those obtained from 32^3 particle simulation

6.4. *Particle turbulent diffusivity*

It can be shown by assuming a diffusion equation for the probability of the displacement of a fluid point (Batchelor 1949) that the turbulent diffusivity, $D_{\mathrm{fp},i}$, in homogeneous turbulence is related to its mean-square displacement via

$$D_{\mathrm{fp},i}(t) = \frac{1}{2}\frac{\mathrm{d}}{\mathrm{d}t}\langle x^2_{\mathrm{fp},i}(t)\rangle. \tag{26}$$

This relation can also be obtained directly using only dimensional arguments (Tennekes & Lumley 1972).

Based on the results of Taylor's theory presented in the preceding section, it is expected that the diffusivities $D_{\mathrm{p},i}$ and $D_{\mathrm{fp},i}$ of the solid particle in zero gravity and its corresponding fluid point to vary linearly with time, for short dispersion times, and be independent of time for long times. Figure 11(*a*), which shows the time development of $D_{\mathrm{p},i}$ and $D_{\mathrm{fp},i}$ for the corn particle in zero gravity, supports this conclusion. Again, as was shown in figure 10(*a*), the solid particles in zero gravity, owing to their finite inertia, disperse laterally faster than their corresponding fluid points.

It is possible to define a turbulent Schmidt number for the dispersion of solid particles as

$$Sc_{\mathrm{p},i} = \frac{D_{\mathrm{fp},i}}{D_{\mathrm{p},i}} = \frac{1}{2}\frac{\mathrm{d}}{\mathrm{d}t}\langle x^2_{\mathrm{fp},i}\rangle \Big/ \frac{1}{2}\frac{\mathrm{d}}{\mathrm{d}t}\langle x^2_{\mathrm{p},i}\rangle, \tag{27}$$

where the diffusivities are those of long dispersion times. In zero gravity, $Sc_{\mathrm{p},1}$ for the corn particle in the lateral direction equals 0.94 (figure 11*a*).

The role of gravity in reducing the turbulent diffusivity in the lateral directions, hence increasing $Sc_{\mathrm{p},i}$ of the solid particles is evident in figure 11(*b*) which shows the developments of $D_{\mathrm{p},1}(t)$ for the corn particle with and without gravity. Also shown are the numerical and experimental $D_{\mathrm{p},1}(t)$ for the glass and copper particles. It is seen that gravity causes $D_{\mathrm{p},1}(t)$ to decrease monotonically with time, after the initial period. The corresponding values of $Sc_{\mathrm{p},1}$ for the corn and copper particles are 4.3 and 55, which are significantly higher than those in zero gravity.

The agreement between the numerical and experimental values of $D_{\mathrm{p},1}(t)$ is good for the corn particle and reasonable for the other particles considering the difficulty in obtaining accurate time-derivatives of $\langle x^2_{\mathrm{p},i}(t)\rangle$ from a photocopy of the published curves of SL.

Figure 11(*c*) displays $D_{\mathrm{p},3}(t)$ for the three particles in the gravity direction. It is evident that $D_{\mathrm{p},3}(t)$ varies linearly with time, indicating that $\langle x^2_{\mathrm{p},3}(t)\rangle \sim t^2$, i.e. parabolic in time as was discussed in §6.3. Consequently, $D_{\mathrm{p},3}(t)$ does not attain an asymptotic value. It is significant to note the relatively large magnitudes of $D_{\mathrm{p},3}(t)$ as compared to $D_{\mathrm{p},1}(t)$ and $D_{\mathrm{p},2}(t)$. Here we recall the discussion in §6.3 concerning

the *true turbulent dispersion* and conclude that only $D_{p,1}(t)$ and $D_{p,2}(t)$ represent the turbulent diffusivity of the solid particle.

6.5. *More about the effects of inertia*

In the preceding sections, the effects of inertia on particle dispersion were discussed by comparing the behaviour of a solid particle in zero gravity to that of the corresponding fluid point. However, the range of particle response times already presented (which is nearly the same as of SL) is relatively narrow. The ratio of the largest $\tau_{p,0}$ to the smallest is 2.48 as shown in table 1. In order to expand this range and see whether the results obtained so far can be safely generalized to cover much heavier particles we performed a simulation for an additional particle whose $\tau_{p,0}$ equals 0.505 s which is 18.7 times that of the corn particle. This new particle can be considered a corn particle of diameter $d = 376$ μm instead of 87 μm of the original corn particle, or a uranium particle ($\rho_p = 19 \times 10^3$ kg/m^3) with diameter $d = 87$ μm. In either case the particle diameter is less than the Kolmogorov lengthscale of our decaying turbulence. In order to facilitate the discussion of the results we will refer to the new particle as the 'uranium particle'. The simulation for the uranium particle is in zero gravity in order to examine the effects of inertia. Since the turbulence is isotropic, only the statistics in the x_1-direction are presented.

Figure 12(*a*) shows the time development of the autocorrelation $R_{Lp,1}$ for the corn, copper and uranium particles, the solid lines labelled A, C and D respectively, and for a fluid point (dashed line). The main difference between $R_{Lp,1}$ of the uranium and the other two particles is that, initially, the bell-shaped curve of the former deviates significantly from that of the fluid point, and later decays faster than the other two. That deviation vanishes at time equal to about 2.75 times $\tau_{p,0}$ of the uranium particle, and as time increases its $R_{Lp,1}$ becomes less than that of the fluid point.

It is appropriate here to distinguish between the effects of inertia and gravity on $R_{Lp,i}$ of heavy particles in isotropic turbulence. Owing to inertia, and for short dispersion times, the magnitude of the autocorrelation of a heavy particle in zero gravity may considerably exceed that of a fluid point. At a time of about one eddy turnover time, $\tau_{f,0}$, the decay of the fluid point autocorrelation starts to level off. The solid particle, again owing to its inertia, continues to interact with new surrounding fluid elements, and thus its $R_{Lp,1}$ decays at a faster rate than that of the fluid point. For example, $R_{Lp,1}$ of the uranium particle becomes less than that of the fluid point at about five eddy turnover times. Consequently, the diffusivity of the heavy particle in zero gravity, $D_{p,1}(t)$, may exceed that of the fluid point initially, but for long times the reverse takes place as shown in figure 12(*b*).

Gravity, on the other hand, reduces $R_{Lp,i}$ of the solid particles relative to that of the fluid points only in the lateral directions and increases it in the gravity direction (figure 9*a*, *b*) as discussed in §6.2. Note that the deviation of $R_{Lp,3}$ from that of the fluid point increases indefinitely (figure 9*b*).

It is therefore evident that gravity always reduces particle dispersion in the lateral directions, whereas inertia may increase dispersion during the initial period and decrease it for longer times, especially for relatively heavy particles with τ_p/τ_f of order 1. Thus the combined effect of the two mechanisms is that the rate of lateral dispersion of a heavy particle, $D_{p,i}(t)$, in gravity environment is always less than that of a fluid point and it decreases monotonically with time as shown in figure 11(*b*).

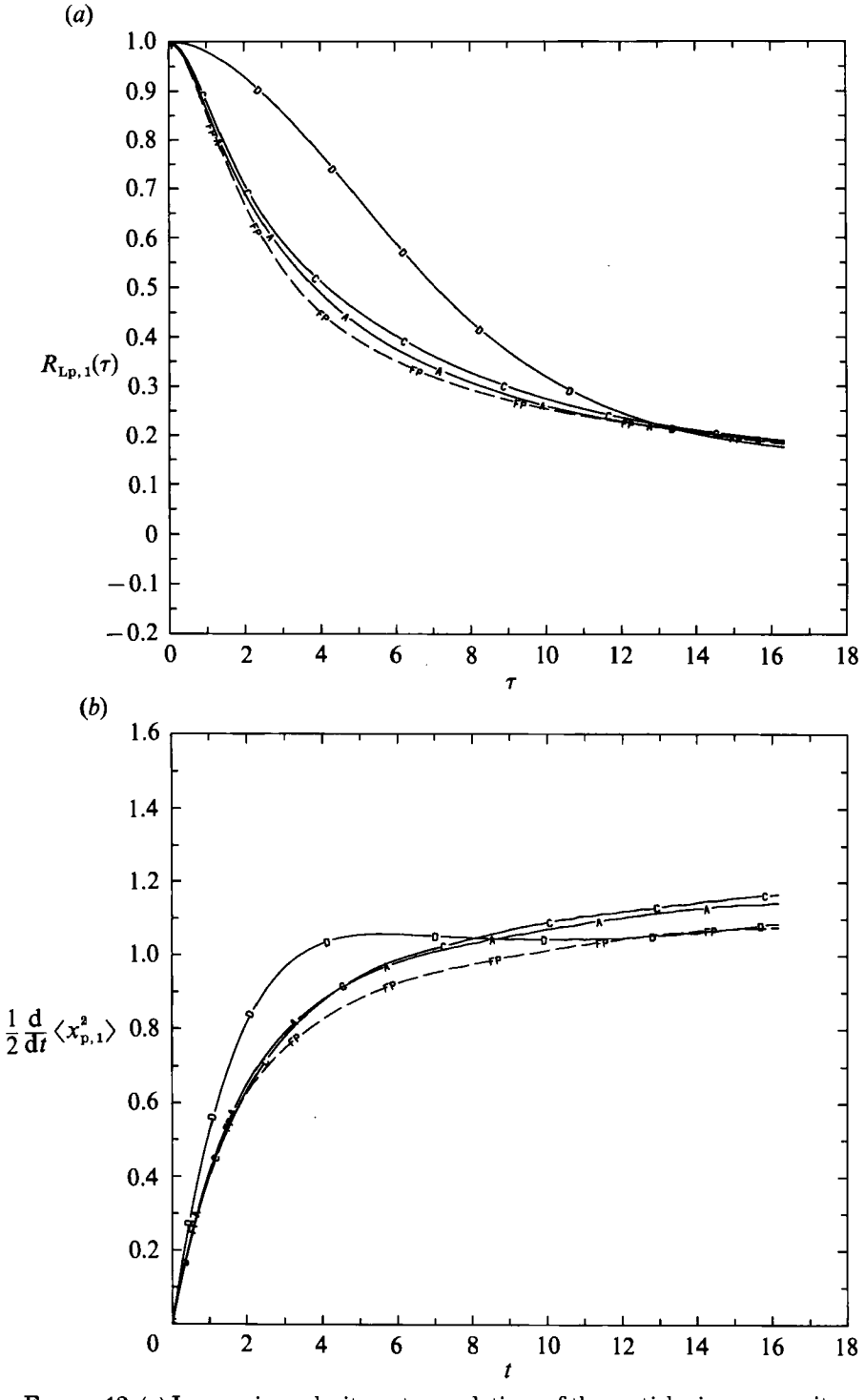

FIGURE 12. (*a*) Lagrangian velocity autocorrelations of the particles in zero gravity and fluid points in the lateral direction (x). A, corn; C, copper; D, uramium; FP, fluid point. (*b*) Normalized turbulent diffusivities in zero gravity, in the lateral direction (x).

6.6. *Lagrangian velocity frequency spectrum*

In this section we discuss the spectral response of a solid particle to the turbulent velocity fluctuation of its surrounding fluid. The approach is to follow the particle, in the time domain, and calculate for both the particle and its host fluid the turbulence energy content at all resolved frequencies. The highest frequency in the spectrum is the Kolmogorov frequency, $\omega_K = \pi/\tau_K$, and the smallest is associated with the large-scale motion. The most suitable quantity for our purpose is the Lagrangian velocity frequency spectrum, $E^L(\omega_n)$, which is the cosine transform of the velocity autocovariance, $R_{ii}(\tau)$, and is defined as:

$$E^L(\omega_n) = \frac{1}{N}\left[2\sum_{j=1}^{N} R_{ii}(t_j)\cos(\omega_n t_j) + R_{ii}(0)\right], \tag{28}$$

where

$$R_{ii}(\tau) = \langle v_i(t_0)\, v_i(t_0+\tau)\rangle, \quad \omega_n = (\pi n)/(N\Delta t), \quad n = 1,\ldots,N, t_j = j\Delta t, \Delta t$$

is the timestep used in integrating (1) and (3) for the particle velocity and position respectively, and N is the total number of timesteps. It should be noted that (28) is strictly valid for statistically stationary turbulence.

In order to distinguish between the effects of inertia and gravity on the frequency spectrum of the particles we compare the spectra in gravity and zero gravity environments.

Only the spectra associated with the lateral velocity in the x_1-direction are presented since they are nearly identical to those in the x_2-direction, and since the turbulent velocity fluctuations in these lateral directions are not overshadowed by the mean drift velocity as is the cae in the x_3-direction.

Figure 13(*a*) shows the spectra for the corn and uranium particles (labelled A and D respectively) and their associated surrounding fluids in zero gravity. We did not include the curves of other particles in order to make the figure easier to read. The abscissa is the frequency normalized by the Kolmogorov frequency, $\omega_K = \pi/\tau_{K,0}$, at the initial time $T = 2.67$ (table 1). It is seen, as expected, that most of the turbulence energy for the fluid and particles is associated with the low-frequency motion. For frequencies higher than the Kolmogorov frequency, i.e. $\omega/\omega_K > 1.0$, all the spectra level off and then oscillate with very small amplitudes. This is due to numerical noise introduced in the spectral mapping of the velocity at the unresolved high frequencies. This also indicates that the sampling time interval is small enough to capture all the spectral information pertaining to the true physical behaviour of the particles and their surrounding fluid.

It is seen, in this zero gravity case, that $E_p^L(\omega)$ of the corn exceeds that of its surrounding fluid at all frequencies except near ω_K. On the other hand, $E_p^L(\omega)$ of the heavier uranium particle is less than its $E_{sf}^L(\omega)$ for medium to high frequencies and exceeds it only at low frequencies. Also the magnitude of deviation between the energies of the particle and its surrounding fluid is higher for the heavier particle. Now, the finding that $E_p^L(\omega)$ can exceed $E_{sf}^L(\omega)$ seems to contradict Csanady's theory (1963) which gives the ratio of the two spectra as

$$\frac{E_p^L(\omega)}{E_{sf}^L(\omega)} = \frac{1}{(1+\tau_p^2\omega^2)}, \tag{29}$$

indicating that $E_p^L(\omega)$ never exceeds $E_{sf}^L(\omega)$. However, (29) was derived for the case of statistically stationary turbulence. In a decaying turbulence, as in our simulation,

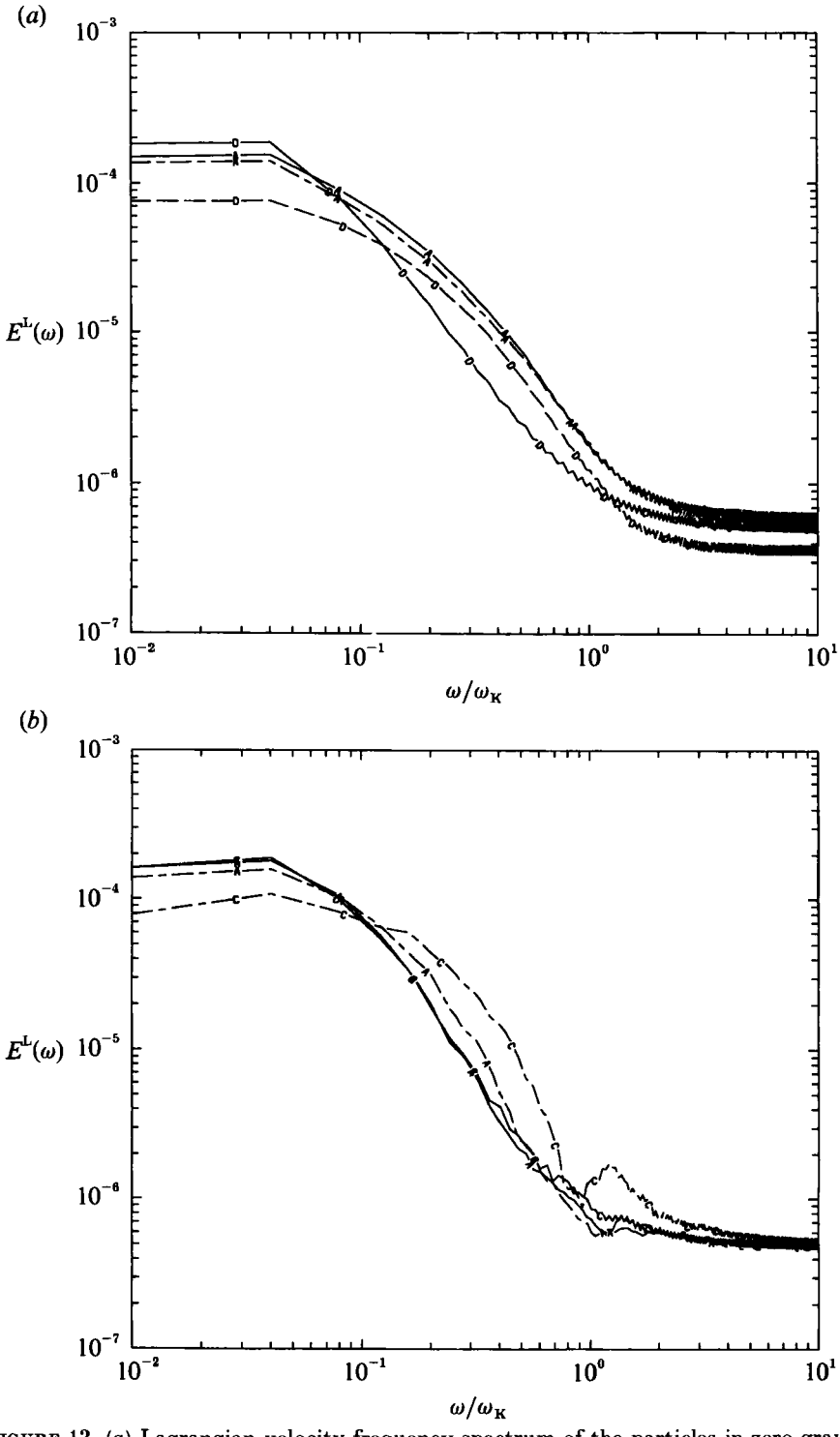

FIGURE 13. (*a*) Lagrangian velocity frequency spectrum of the particles in zero gravity and their corresponding surrounding fluid. A, corn; D, uranium. ——, particles; – – –, surrounding fluid for corn; – – – –, surrounding fluid for uranium. (*b*) Lagrangian velocity frequency spectrum of the particles in gravity and their corresponding surrounding fluid. C, copper.

Particle	$\omega_{f,0} = v_{t,0}/l_0(s^{-1})$	$1/\tau_{p,0}(s^{-1})$
Corn	9.75	37.0
Copper	20.73	14.9

TABLE 5. $\omega_{f,0}$ and $1/\tau_{p,0}$ for Csanady's inequality

the decay rate of the kinetic energy of particles, owing to their finite inertia, is less than that of the surrounding fluid especially during the initial period of dispersion. As discussed in §6.1, the higher the inertia of the particles, the higher is their relative velocity and the smaller the rate of decay of their kinetic energy.

Indeed the source of energy for the low-frequency part of the spectrum of a heavy particle is its highly correlated (large $R_{ii}(\tau)$) velocity due to its finite inertia. In the corresponding part of the surrounding fluid spectrum, $E^{L}_{sf}(\omega)$, which is associated with the large-scale motion, the energy results from the less correlated velocity of the host fluid whose identity changes continuously along the particle path, and whose energy decays with time, hence the lower energy. Now, at higher frequencies, the heaviest particle (uranium), owing to its relatively large τ_p, is unable to follow the fluid velocity fluctuations, hence the lower value of $E^{L}_{p}(\omega)$ as compared to $E^{L}_{sf}(\omega)$. On the other hand, $E^{L}_{p}(\omega)$ of the lighter particle follows closely its $E^{L}_{sf}(\omega)$ and even exceeds it in magnitude. Again, Csanady's relation (29) would not be able to predict these results.

In the gravity case, figure 13(*b*) shows the spectra of the corn and copper particles and their surrounding fluid. At the low-frequency end, we observe the same behaviour as in the zero gravity case, i.e. the particle energy is higher than that of the surrounding fluid.

At medium and high frequencies, it is seen that gravity reduces the particle energy relative to that of the surrounding fluid. Thus the effect of gravity on particle response to fluid turbulence is frequency sensitive, with most of the reduction of particle energy relative to that of the surrounding fluid occurring at medium and high frequencies. The reverse takes place at lower frequencies.

We also compared the energies E_p and E_{sf}, where

$$E_p = \int_0^\infty E^{L}_{p}(\omega)\,d\omega, \tag{30}$$

$$E_{sf} = \int_0^\infty E^{L}_{sf}(\omega)\,d\omega, \tag{31}$$

and found, for both the corn and copper particles, that E_p is higher than E_{sf}. However, this is mainly due to the energy content of the lower-frequency part of the spectrum where most of the energy resides. The contribution of the high-frequency part of the spectrum to the energy is not significant.

Csanady (1963) hypothesized that if $\omega_f \ll 1/\tau_p$, where $\omega_f = v_t/l$ is the typical frequency of the fluid based on the turbulence lengthscale and the terminal velocity of the particle, v_t, then the response time of the particle is sufficiently small for the particle to follow the fluctuations of its surrounding fluid. Table 5 shows that Csanady's inequality is satisfied for the corn particle but not for the copper, and thus the results of figure 13(*b*) support Csanady's hypothesis qualitatively.

(a)

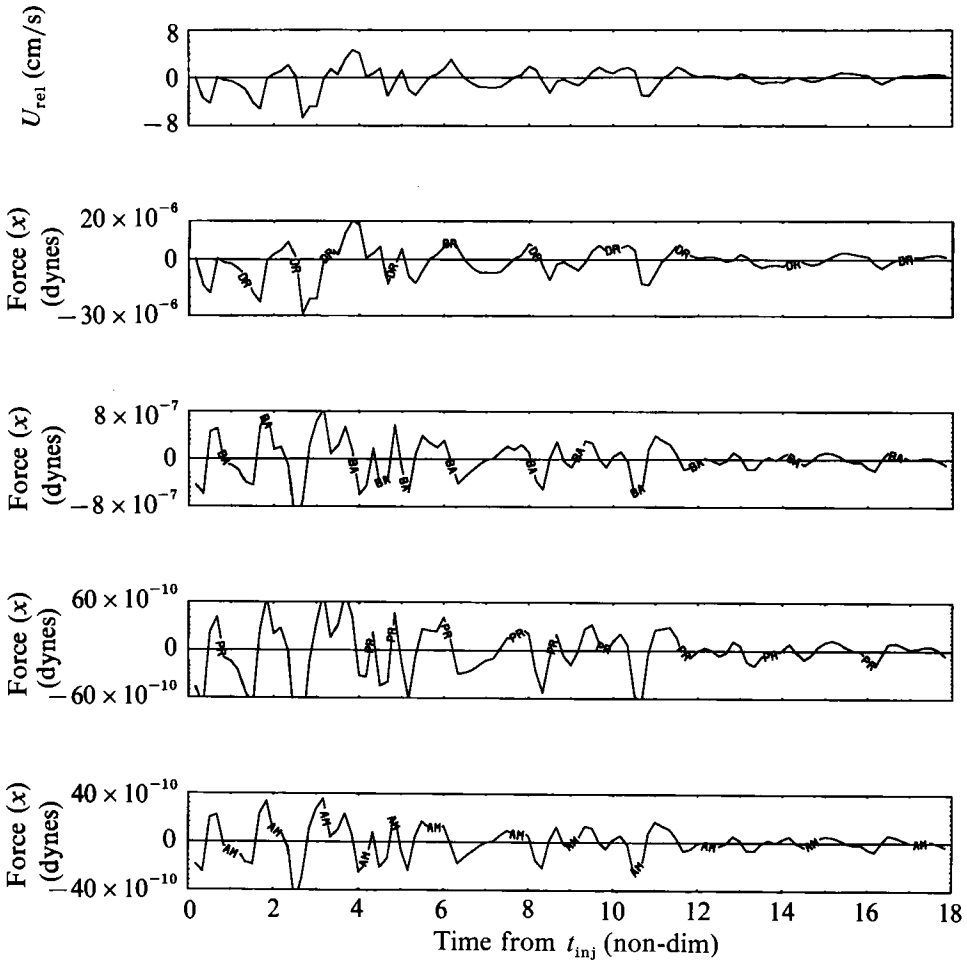

FIGURE 14(a). For caption see p. 697.

6.7. *Time development of all the forces acting on a solid particle*

The purpose of this section is to present the time development of all the forces acting on *one* copper particle starting from the time of its injection into the decaying turbulence in gravity environment. The reason for presenting the instantaneous forces on one particle only and not the ensemble average of the forces on all the 22^3 particles is as follows. The forces change their sign continuously depending on the relative velocity (see (1)). Thus, for a large enough number of particles in homogeneous isotropic turbulence, the positive and negative values would tend to cancel out, and the resulting ensemble mean force, except that due to gravity, would approach zero.

The components in the three directions of the drag and Basset forces, and those due to pressure gradient, added mass and gravity are presented first (in dynes) without normalizing to provide a set of 'raw data' that can be of benefit to

(*b*)

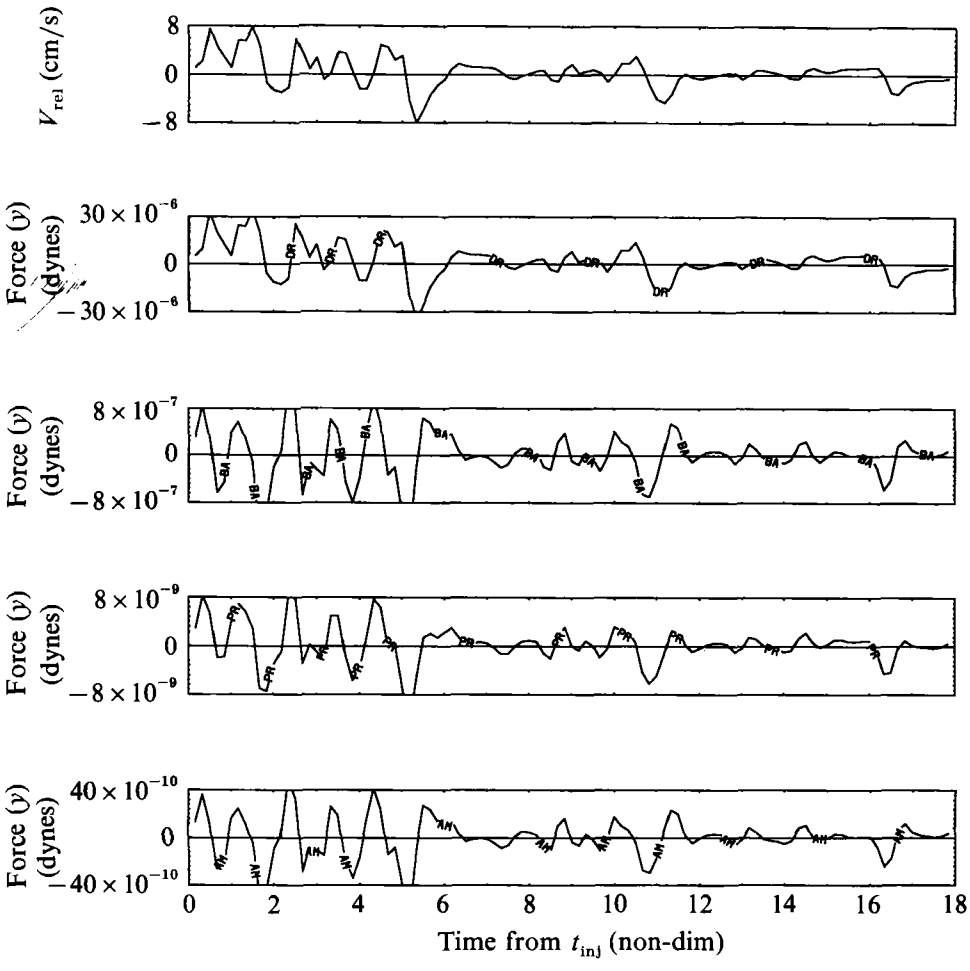

FIGURE 14(*b*). For caption see p. 697.

experimentalists and developers of mathematical models. Secondly, the forces in a given direction are normalized by the drag in that direction to examine their relative significance.

Figures 14(*a*), 14(*b*) and 14(*c*) display the time development of the forces, in the x_1, x_2 and x_3 directions, respectively, acting on one copper particle, selected randomly from the total of 10648 particles tracked. Figures 14(*d*), 14(*e*) and 14(*f*) show the forces normalized by the drag. As explained in §2, the forces acting on each of the 22^3 particles are calculated at each timestep from the instantaneous velocities of the particle and its surrounding fluid.

The following observations can be made from figure 14(*a–f*):

(i) The amplitudes of the fluctuations of the relative velocities and forces in the lateral directions (x_1 and x_2) diminish with time, indicating that the particle velocity is asymptotically approaching that of the decaying turbulence as discussed in §6.1.

(ii) The buoyancy force is about three times the drag in the gravity direction. In

(c)

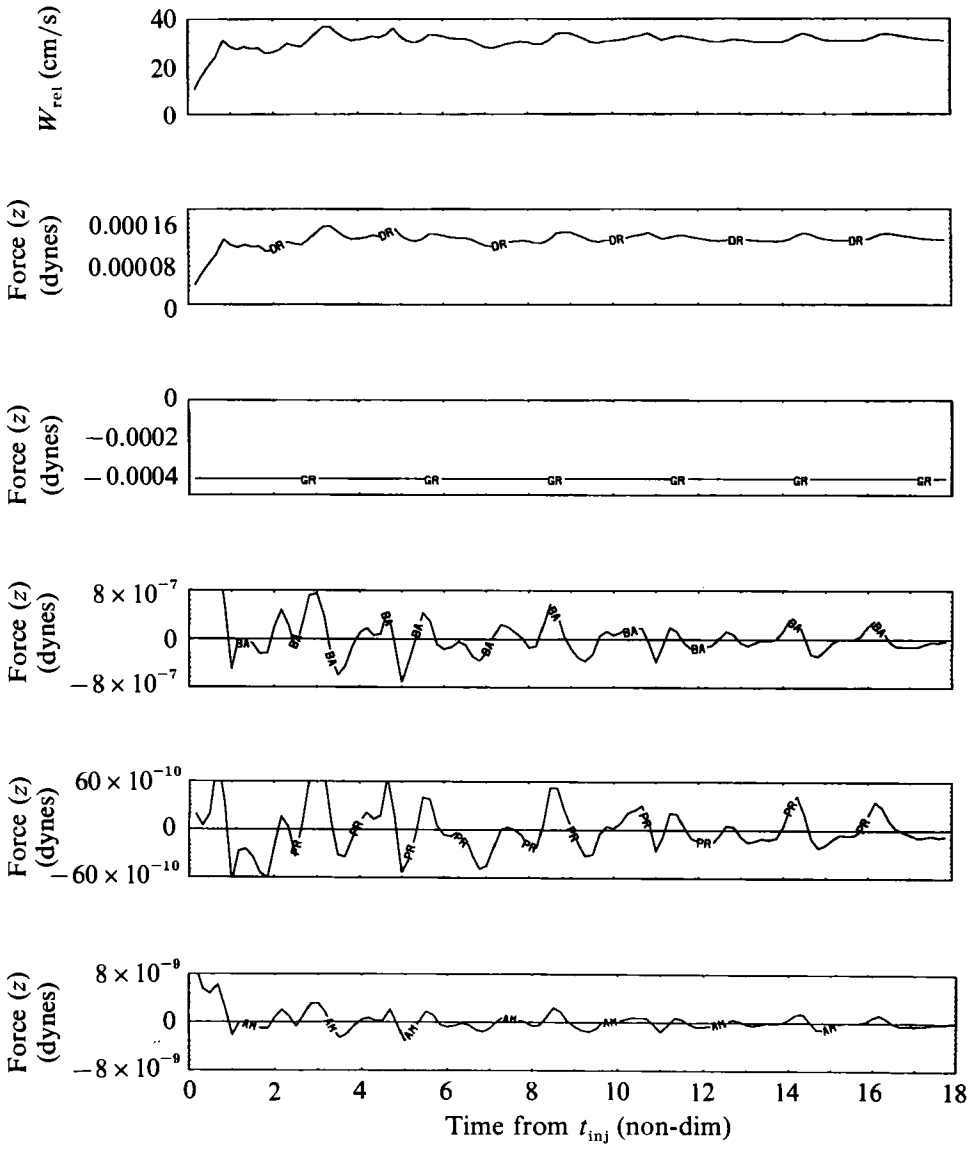

FIGURE 14(c). For caption see p. 697.

the lateral directions, the drag and Basset forces are the main forces although the former is at least one order of magnitude higher than the latter.

(iii) The extremely high magnitudes ($\gg 1$) of the normalized forces correspond to the instances of nearly zero drag (i.e. zero relative velocity) and should be ignored as singularities since the magnitudes of these forces in dynes are orders of magnitude less than the drag.

In order to determine the effect of including the pressure, added mass, and Basset forces in (1) on the particle dispersion statistics, a simulation with only the drag and gravity forces was performed for the corn and copper particles. Table 6 lists the maximum percentage differences in the dispersion statistics of a simulation (*a*) with

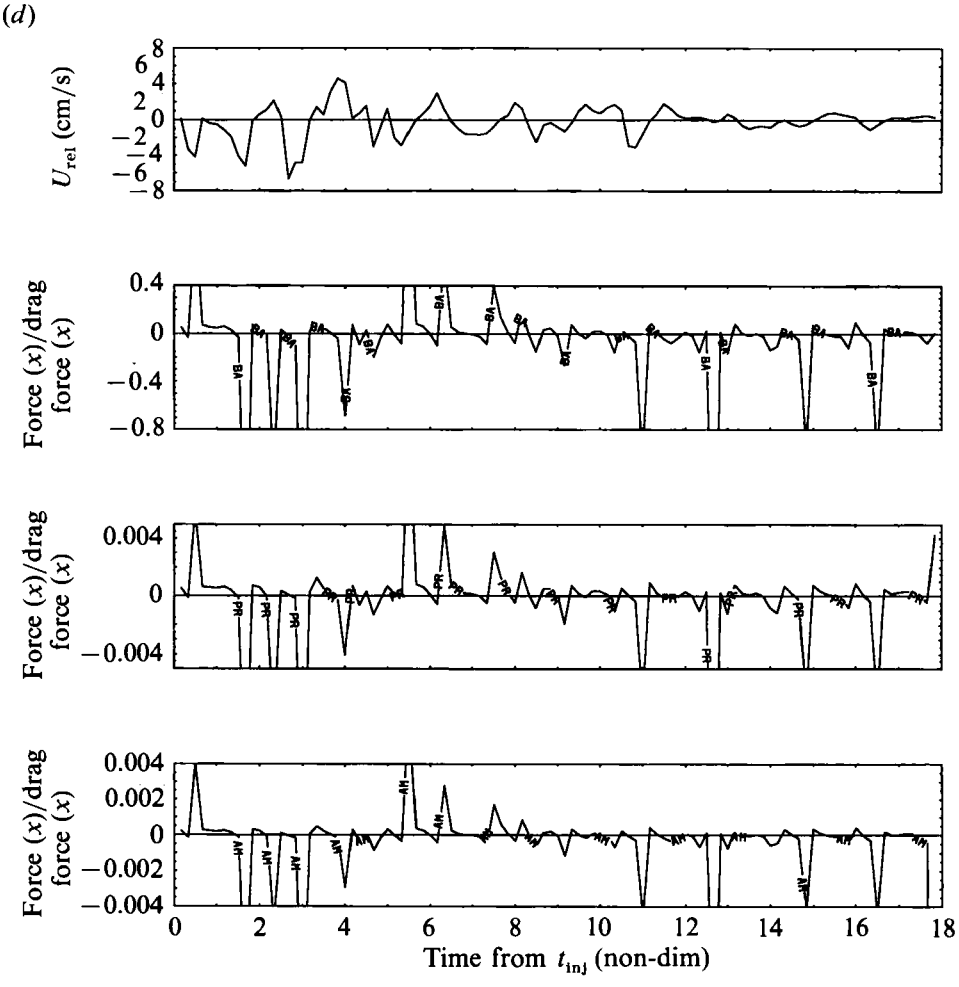

FIGURE 14(*d*). For caption see p. 697.

only the drag and gravity forces included, with respect to another simulation (*b*) with all the five forces included. The maximum difference shown in table 6 is 3.8% for the Lagrangian integral timescale. This difference is due to the inclusion of the Basset force in the particle motion equation since the pressure gradient and added mass forces are one to three orders of magnitude smaller than the Basset force, as indicated in figure 14(*a–f*).

7. Conclusions

We presented a numerical method by which the three-dimensional, time-dependent velocity field of a homogeneous, isotropic decaying turbulence was computed directly (DNS). A numerical grid containing 96^3 points was sufficient to resolve the turbulent motion at the Kolmogorov lengthscale ($1.15 \leqslant \eta k_{max} \leqslant 3$) for a range of microscale Reynolds numbers starting from $R_\lambda = 25$ and decaying to $R_\lambda = 16$. The dispersion characteristics of three different solid particles (corn, copper and glass) injected in the isotropic non-stationary flow, were obtained by integrating the

(e)

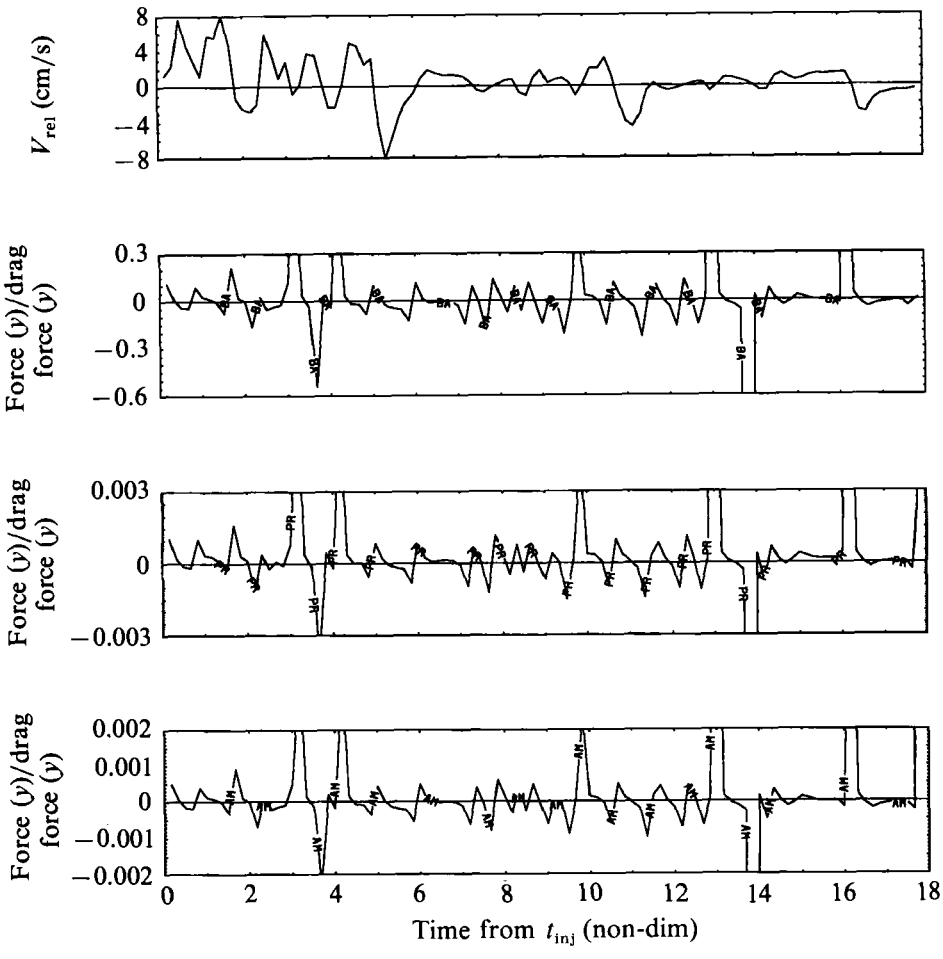

FIGURE 14 (e). For caption see facing page.

Parameter	Corn	Copper
T_{L_x}	3.8%	1.6%
T_{L_y}	3.8%	1.5%
T_{L_z}	−0.3%	−0.1%
$\langle x^2_{p,1} \rangle$	0.5%	0.2%
$\langle x^2_{p,2} \rangle$	0.2%	0.2%
$\langle x^2_{p,3} \rangle$	−0.1%	0.0%
$\langle v^2_{rel,1} \rangle_{(peak)}$	−3.0%	−2.0%
$\langle v^2_{rel,2} \rangle_{(peak)}$	−3.0%	−2.0%

TABLE 6. Percentage differences between simulations (a) and (b) for various Lagrangian statistics

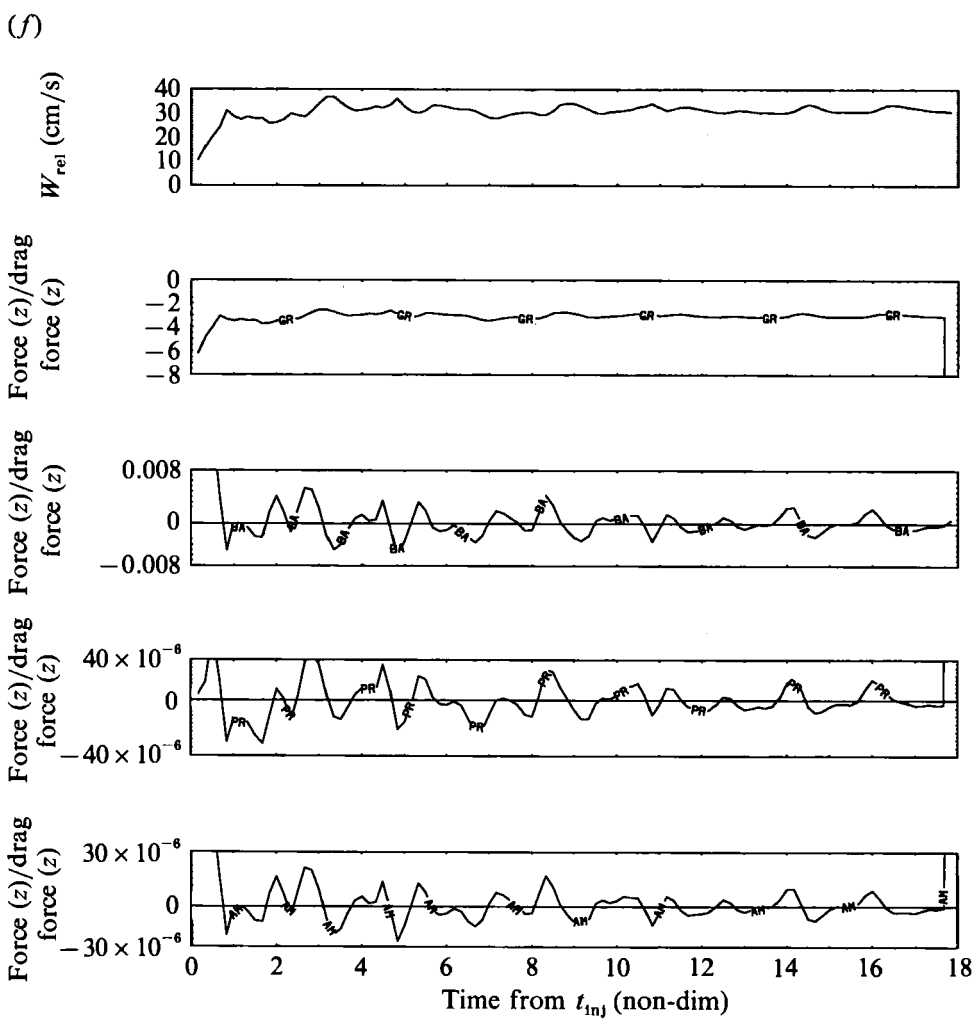

FIGURE 14. Forces (dynes) on the copper particle (*a*) in the lateral direction (*x*), (*b*) in the lateral direction (*y*), (*c*) in the gravity direction (*z*), (*d*) in the lateral direction (*x*) normalized by the drag force, (*e*) in the lateral direction (*y*) normalized by the drag force, (*f*) in the gravity direction (*z*) normalized by the drag force. DR, drag; BA, Basset; PR, fluid pressure gradient; AM, added mass; GR, gravity.

complete equation of particle motion, (1), along the instantaneous trajectories of 22^3 particles for each particle type, and then performing ensemble averaging. The three different particles were those used by Snyder & Lumley (1971), referred to throughout the paper as SL. Because of the lower Reynolds number in DNS, certain scaling of the relevant timescales is necessary (12) and (13)).

Good agreement was achieved between our DNS results and SL measurements for the time development of the mean-square displacement of the particles. This agreement indicates first that although R_λ in our simulation is about a third of that in the experiment, there is sufficient nonlinear interaction between the resolved wavenumbers to simulate 'real' turbulence (figure 3). Secondly, the numerical time integration of the Lagrangian motion equation (1) of the particle, including the

Hermitian interpolation scheme for calculating the velocity of its surrounding fluid, is quite accurate. Thirdly, the statistics of particle dispersion obtained from the ensemble of 22^3 particle trajectories is of acceptable accuracy.

The simulation results also include the time development of the mean-square relative velocity of the particles, the Lagrangian velocity autocorrelation and the turbulent diffusivity of the particles and fluid points. The Lagrangian velocity frequency spectra of the particles and their surrounding fluid, as well as the time development of all the forces acting on one copper particle are also presented. In order to distinguish between the effects of inertia and gravity on the dispersion statistics we compare the results of simulations made with and without the gravity force included in (1).

The main objective of the paper is to enhance the understanding of the physics of particle dispersion in a simple turbulent flow by examining the simulation results described above and answering the questions of how and why solid particles behave the way they do. Some of the interesting findings of the work is summarized below.

(i) The crossing trajectories (Yudine 1959) and the continuity effect (Csanady 1963) associated with it are manifested in the occurrence of negative loops in the Lagrangian velocity autocorrelations of heavier particles in the lateral directions. These negative loops do not exist in zero gravity.

(ii) For all particles in gravity environment, the magnitudes of the Lagrangian autocorrelations of the surrounding fluid are less than those of particles, and the higher the response time of the particle, the lower is the autocorrelation of the surrounding fluid.

(iii) The 'true' effects of turbulence on solid particle dispersion can be 'seen' only in the lateral directions since the drift velocity can overshadow the turbulent velocity fluctuations.

(iv) The theory of Taylor (1921) on the turbulent diffusion of fluid points can be applied directly to solid particles in zero gravity. Large deviations from the theory occur for long dispersion times in gravity environment owing to the crossing trajectories effect (figure 10*f*). This effect manifests itself in the decay of the product $\langle v_i^2 \rangle R_\tau$, and not just in the decrease of R_τ.

(v) The inertia of a solid particle may cause its turbulent diffusivity in zero gravity to exceed that of its corresponding fluid point, i.e. the turbulent Schmidt number of a particle in zero gravity is less than unity, for short dispersion times. For long dispersion times, in zero gravity, the diffusivities of both reach asymptotic values, in agreement with Taylor's theory. In gravity environment, and for long times, the turbulent diffusivity of a solid particle, in the lateral directions, decreases monotonically thus eventually increasing its turbulent Schmidt number by orders of magnitude above that in zero gravity. This reduction of lateral dispersion of the particle at long times is due to both inertia and gravity.

(vi) The Lagrangian velocity frequency spectra of the particles in zero gravity show that at low frequencies, the turbulence energy of each of the considered particles exceeds that of the corresponding surrounding fluid. This result contradicts Csanady's theory (1963), for the ratio of particle energy to that of the surrounding fluid, when used in decaying turbulence.

In gravity environment, the ratio of particle energy to that of the surrounding fluid is frequency sensitive. That is, gravity reduces particle energy at medium and high frequencies, in the lateral directions, below that of the surrounding fluid. The reverse takes place at lower frequencies where particle energy becomes higher than that of the surrounding fluid.

(vii) The study of the time development of all the forces acting on a solid particle shows that in the gravity direction the buoyancy and drag forces dominate the particle behaviour, and the former may exceed the latter. In the lateral directions, the drag and Basset forces are the main forces although the former is at least one order of magnitude higher than the latter.

The computations presented in this paper have been performed on the supercomputers Cray XMP/48, Cray YMP and Cray 2 at two computer centres whose support is greatly acknowledged and without which this work could not have been accomplished. These centres are the San Diego Supercomputer Center (SDSC) and the Numerical Aerodynamic Simulation (NAS) at NASA-Ames. This work was also supported in part by the University of California, Irvine, through an allocation of computer time on the Convex-C240 supercomputer.

REFERENCES

AUTON, T. R. 1983 The dynamics of bubbles, drops and particles in motion in liquids. PhD thesis, Cambridge University.

BALACHANDAR, S. & MAXEY, M. R. 1989 Methods for evaluating fluid velocity in spectral simulations of turbulence. *J. Comput. Phys.* **115**, 1569–1579.

BASSET, A. B. 1888 *A Treatise on Hydrodynamics*, vol. 2, p. 285. Dover.

BATCHELOR, G. K. 1949 Diffusion in a field of homogeneous turbulence. *Austal. J. Sci. Res.* A **2**, 437–450.

BATCHELOR, G. K. 1953 *The Theory of Homogeneous Turbulence*. Cambridge University Press.

BOUSSINESQ, J. 1903 *Theorie Analytique de la Chaleur*, vol. 2, p. 224. Paris.

CORRSIN, S. & LUMLEY, J. L. 1956 On the equation of motion for a particle in turbulent fluid. *Appl. Sci. Res.* **6**, 114–116.

CROWE, C. T., CHUNG, J. N. & TROUT, T. R. 1988 Particle mixing in free shear flows. *Prog. Energy Combust. Sci.* **14**, 171–194.

CSANADY, G. T. 1963 Turbulent diffusion of heavy particles in the atmosphere. *J. Atmos. Sci.* **20**, 201–208.

ELGHOBASHI, S. E. & TRUESDELL, G. C. 1989*a* Direct simulation of particle dispersion in grid turbulence and homogeneous shear flows. *Bull. Am. Phys. Soc.* **34**, 2311.

ELGHOBASHI, S. E. & TRUESDELL, G. C. 1989*b* Direct simulation of particle dispersion in a decaying isotropic turbulence. *Seventh Symp. on Turbulent Shear Flows*, M, pp. 121–122.

ELGHOBASHI, S. E. & TRUESDELL, G. C. 1991 On the interaction between solid particles and decaying turbulence. *Eighth Symp. on Turbulent Shear Flows*, vol. 1, pp. 731–736.

GERZ, T., SCHUMANN, U. & ELGHOBASHI, S. E. 1989 Direct simulation of stably stratified homogeneous turbulent shear flows. *J. Fluid Mech.* **200**, 563–594.

KANEDA, Y. & GOTOH, T. 1991 Lagrangian velocity autocorrelation in isotropic turbulence. *Phys. Fluids* A **3**, 1924–1933.

KRAICHNAN, R. H. 1970 Diffusion by a random velocity field. *Phys. Fluids* **13**, 22–31.

LUMLEY, J. L. 1957 Some problems connected with the motion of small particles in a turbulent fluid. PhD thesis, Johns Hopkins University: 41.

LUMLEY, J. L. 1978 Two-phase and non-newtonian flows. *Topics Phys.* **12**, 290–324.

MCLAUGHLIN, J. B. 1989 Aerosol particle deposition in numerically simulated channel flow. *Phys. Fluids* A **1**, 1211–1224.

MAXEY, M. R. & RILEY, J. J. 1983 Equation of motion for a small rigid sphere in a nonuniform flow. *Phys. Fluids* **26**, 883–889.

MOHAMED, M. S. & LARUE, J. C. 1990 The decay power-law in grid generated turbulence. *J. Fluid Mech.* **219**, 195–214.

MONIN, A. S. & YAGLOM, A. M. 1979 *Statistical Fluid Mechanics*, vol. 1, pp. 540–550. The MIT Press.

ORSZAG, S. A. & PATTERSON, G. S. 1972 Numerical simulation of three-dimensional homogeneous turbulence. *Phys. Rev. Lett.* **28**, 76–79.

OSEEN, C. W. 1927 Über die stokes'sche formel, und über eine verwandte aufgabe in der hydrodynamik. *Hydromechanik* **82**. Leipzig.

PAO, Y.-H. 1965 Structure of turbulent velocity and scalar fields at large wavenumbers. *Phys. Fluids* **8**, 1063–1075.

REEKS, M. W. 1977 On the dispersion of small particles suspended in an isotropic turbulent fluid. *J. Fluid Mech.* **83**, 529–546.

RILEY, J. J. & PATTERSON, G. S. 1974 Diffusion experiments with numerically integrated isotropic turbulence. *Phys. Fluids* **17**, 292–297.

SCHUMANN, U. 1977 Realizability of Reynolds-stress turbulence models. *Phys. Fluids* **20**, 721–725.

SCHUMANN, U. & PATTERSON, G. S. 1978 Numerical study of pressure and velocity fluctuation in nearly isotropic turbulence. *J. Fluid Mech.* **88**, 685–709.

SHLIEN, D. J. & CORRSIN, S. 1974 A measurement of Lagrangian velocity autocorrelation in approximately isotropic turbulence. *J. Fluid Mech.* **62**, 255–271.

SNYDER, W. H. & LUMLEY, J. L. 1971 Some measurements of particle velocity autocorrelation functions in a turbulent flow. *J. Fluid Mech.* **48**, 41.

SQUIRES, K. D. & EATON, J. K. 1991 Measurements of particle dispersion obtained from direct numerical simulations of isotropic turbulence. *J. Fluid Mech.* **226**, 1–35.

STOKES, G. C. 1851 On the effect of the internal friction of fluids on the motion of pendulums. *Trans. Camb. Phil. Soc.* **9**, 8.

TAYLOR, G. I. 1921 Diffusion by continuous movement. *Proc. Lond. Math. Soc.* A **20**, 196–212.

TCHEN, C. M. 1947 Mean value and correlation problems connected with the motion of small particles suspended in a turbulent fluid. PhD thesis, Delft University. The Hague: Martinus Nijhoff.

TENNEKES, H. & LUMLEY, J. L. 1972 *A First Course in Turbulence.* The MIT Press.

TOWNSEND, A. A. 1976 *The Structure of Turbulent Shear Flow*, p. 340. Cambridge University Press.

TRUESDELL, G. C. 1989 A study of two-dimensional interpolation schemes. *Rep. no.* FTS/89-1, Mechanical Engineering Department, University of California, Irvine.

WELLS, M. R. & STOCK, D. E. 1983 The effects of crossing trajectories on the dispersion of particles in a turbulent flow. *J. Fluid Mech.* **136**, 31–62.

YEUNG, P. K. & POPE, S. B. 1988 An algorithm for tracking fluid particles in numerical simulations of homogeneous turbulence. *J. Comp. Phys.* **79**, 373–415.

YUDINE, M. I. 1959 Physical considerations on heavy-particle diffusion. *Adv. Geophys.* **6**, 185–191.